CODED APERTURE IMAGING IN X- AND GAMMA-RAY ASTRONOMY

E. CAROLI, J. B. STEPHEN, G. DI COCCO, L. NATALUCCI, and A. SPIZZICHINO

Istituto TE.S.R.E./C.N.R., Via de' Castagnoli 1, Bologna, Italy

(Received 6 August, 1987)

Abstract. Coded aperture imaging in high energy astronomy represents an important technical advance in instrumentation over the full energy range from X- to γ-rays and is playing a unique role in those spectral ranges where other techniques become ineffective or impracticable due to limitations connected to the physics of interactions of photons with matter. The theory underlying this method of indirect imaging is of strong relevance both in design optimization of new instruments and in the data analysis process. The coded aperture imaging method is herein reviewed with emphasis on topics of mainly practical interest along with a description of already developed and forthcoming implementations.

Table of Contents

Space Science Reviews **45** (1987) 349–403.

1. Introduction

In comparison to other branches of astronomy (e.g., optical), the production of sky images in the fields of X- and γ-rays is greatly hindered by two main practical limitations:

(a) the general difficulty in focussing high energy photons and

(b) the weakness of the fluxes with respect to the background counting rate.

In the region of high-energy γ-rays ($E > 50$ MeV), where the pair production mechanism dominates, sky images can be obtained by the use of spark chambers (Derdeyn *et al.*, 1972; Bignami *et al.*, 1975; Parlier *et al.*, 1977; Fichtel *et al.*, 1983) or drift chambers (Crannel and Maurer, 1977; McKechnie *et al.*, 1977), wherein the direction of each detected event may be either evaluated by extrapolating back the spark tracks or calculated by measuring the direction of the electron-positron pair created by the conversion of the photon. At slightly lower energies astronomical images have been produced by double Compton telescopes (Schönfelder *et al.*, 1982, 1984; Hartman *et al.*, 1983; Simone *et al.*, 1985), in which information on the flux direction can be inferred from the analysis of pairs of events in coincidence generated by a Compton scattered photon interacting in two different position sensitive detection planes. All these types of instruments lead to an angular resolution ranging typically from a half degree to a few degrees. At X-ray energies sky images can be obtained using concentrating techniques based on grazing incidence reflection ($E < 15$ keV) (Willingale, 1984; Aschenbach, 1985, and references therein) or Bragg diffraction (Byrnak *et al.*, 1985; Schnopper and Byrnak, 1985) which is potentially effective up to the hard X-ray region (Lund, 1986a; De Chiara and Frontera, 1987). Although these telescopes provide a good angular resolution ($\approx 10''$), they require sophisticated manufacturing techniques and suffer from an unfavourable mass/aperture ratio.

In recent years an increasing interest has been shown in a different class of telescopes based on multiplexing techniques for use in a range of astronomical applications. In these instruments the image formation consists of a two-step procedure:

(a) the modulation of the incident radiation by a suitable configuration of absorbing (opaque) and non-absorbing (transparent) elements;

(b) the implementation of computer algorithms to reconstruct the object scene from the detected events.

These instruments may be conveniently divided into two subclasses. In the first of these the detector is not position-sensitive and the information on the object position is obtained by time multiplexing the signal either by means of one or more collimators or grids rotating over the detector (Bradt *et al.*, 1968; Durouchoux *et al.*, 1983; Theinhardt *et al.*, 1984; Frontera *et al.*, 1984; Lund, 1986b) or by linearly scanning an aperture consisting of a pattern of blocking and transmitting elements (a mask) in front of it (Proctor, 1981; Rocchia *et al.*, 1985). The second class of telescopes utilizes the spatial multiplexing that can be obtained either from using pairs of widely separated collimator grids to form modulation patterns of the incident γ-rays onto a position sensitive detector (PSD), or with one or more arrays of transparent and opaque elements, whose shadow projected along the flux direction is intercepted by a PSD. In the first case we refer to Fourier-transform imagers (Chou and Barrett, 1978; Palmer and Prince, 1987), while the multiplexing instruments of the second kind are known as 'coded mask systems', and have already been used successfully in several other fields: for monitoring confinement fusion experiments (Fenimore *et al.*, 1979; Yamanaka *et al.*, 1984), in nuclear medicine, particularly in tomography (Cannon and Fenimore, 1979; Knoll *et al.*, 1984, Ohyama *et al.*, 1984), in chemical spectroscopy (Harwit *et al.*, 1974; Plankey *et al.*, 1974) and in optical image processing (Oliver, 1976).

Herein we present a review of some general problems related to the use of coded mask instruments, drawn both from contemporary literature and from experience in the field acquired in the development of a coded mask telescope (Baker *et al.*, 1983a, b) for low energy γ-ray astronomy.

2. Principles of Coded Aperture Imaging

In coded aperture imaging systems a mask consisting of an array of opaque and transparent elements is set between the source fluxes and a position sensitive detection plane. Every source, or source element, within the field of view projects a shadow of the aperture on to the detection plane (Figure 2.1). Thus for a single point source the detected two-dimensional distribution of events reproduces a mask pattern, or part of one, while for a more complex source or arrangement of point sources the recorded shadowgram is the sum of many such distributions. For each flux direction the part of the mask that contributes to the coding on the position sensitive detector is called a

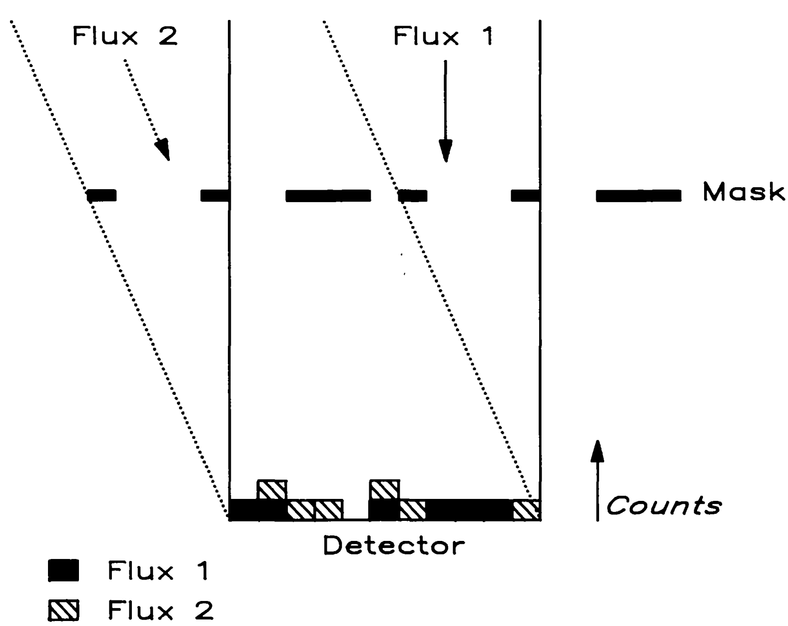

Fig. 2.1. A schematic diagram illustrating the working principle of a Coded Aperture telescope: the recorded count rate in each pixel of the detection plane is the summation of contributions from each source flux modulated by the mask. In particular the shadows generated by two sources at infinite distance from the mask-detector system – one on axis and the other at the edge of the field of view are shown.

'working zone'. Of course, the general requirement is that for every direction the working zone has to be different so as to avoid ambiguities in the reconstruction of the source position.

For any particular telescope geometry the field of view consists of two distinct regions: the Fully Coded Field of View (FCFV) which is defined as comprising all directions for which the detected flux is completely modulated by the mask, and the Partially Coded Field of View (PCFV) in which only a fraction of the detected photons is coded by the aperture pattern (Figure 2.2). The PCFV is also known as the vignetted field of view.

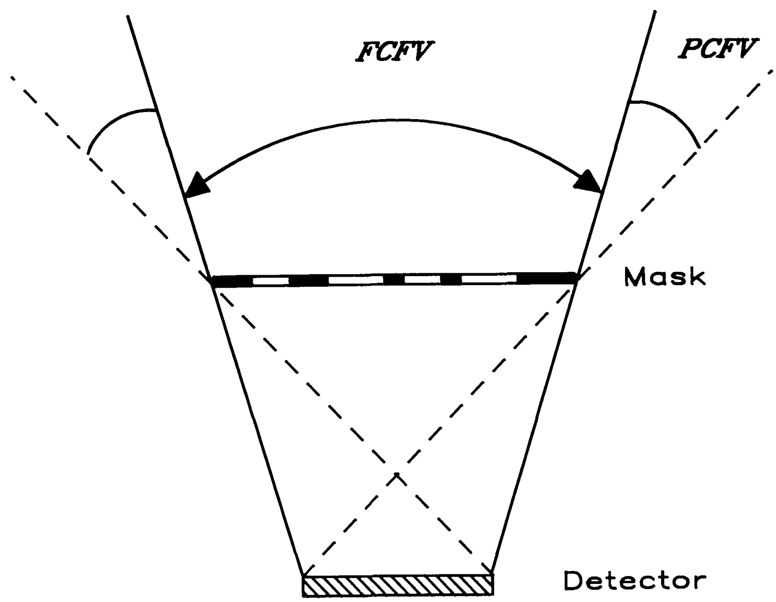

Fig. 2.2. The Fully Coded Field of View (FCFV) is defined as comprising all directions for which the recorded flux is completely modulated by the mask. The Partially Coded Field of View (PCFV) is defined as comprising all the directions for which only a fraction of the detected flux is coded by the mask. The FCFV and the PCFV are shown for a geometrical configuration having the mask larger than the PSD.

In general three different geometric arrangements of a detector-mask system are practical, as shown schematically in Figure 2.3. The simplest arrangement is to have the mask and the PSD of equal dimensions. However, this configuration suffers from the fact that the entire FOV, except for the on-axis direction, is only partially coded. An alternative method which overcomes this problem is to employ a PSD which is larger than the aperture resulting in a wider FCFV. For γ-ray Astronomy, a more practical geometry is depicted in Figure 2.3(c), in which the mask is considerably larger than the PSD. The advantage this provides over the arrangement (b) comes from the ability to have the same FCFV while employing a smaller detection plane. In general for this geometry, the aperture consists of a two by two mosaic of a basic mask pattern, with one row and one column excluded in order to avoid intrinsic ambiguities. This provides a uniform sensitivity over the entire FCFV because the overall transparency of the working zone for each direction is constant. In the case of X-ray astronomy, however,

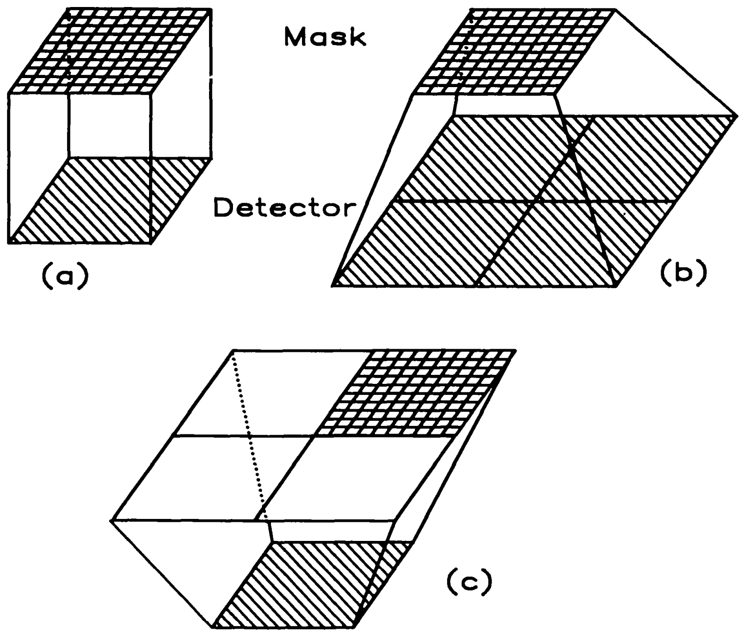

Fig. 2.3. Three possible mask/detector arrangements. (a) The mask and the detector have the same size. (b) The detector dimensions are larger than those of the mask. This configuration provides a larger FCFV. (c) The mask, based on a 2×2 mosaic of the same basic pattern, is larger than the detector. This arrangement provides the same FCFV as (b) while employing a smaller PSD.

where the use of suitable shielding can reduce the dominant source of background to the diffuse emission seen through the mask, arrangement (a) of Figure 2.3 can provide a more favourable signal to noise ratio (SNR) for wide field imaging (Sims *et al.*, 1984).

2.1. Image formation using a mask

As coded aperture imaging is a linear technique, if we denote by $S(x, y)$ the object distribution (we will assume a two-dimensional object as the z-direction is not important for astronomical applications) and by $A(x, y)$ the aperture transmission function, the spatial distribution of the detected flux is mathematically described by:

$$D(x, y) = A(x, y) * S(x, y) + B(x, y), \tag{2.1}$$

where $*$ is the convolution operator and $B(x, y)$ is a signal-independent noise term. An estimate $\hat{S}$ of the object S can thereafter be obtained by filtering the shadowgram D with a suitable decoding function $G(x, y)$:

$$\hat{S}(x, y) = G(x, y) * A(x, y) * S(x, y) + G(x, y) * B(x, y). \tag{2.2}$$

The quality of the object reconstruction therefore depends on the choice of the aperture $A(x, y)$ and the decoding function G (Groh *et al.*, 1972; Brown, 1974; Cannon and Fenimore, 1980).

When the modulation of the incident fluxes is obtained by means of a coded mask consisting of N elements of equal size and shape, M of which are transparent, the aperture A may be considered as a series of step functions. The transmission function $A(x, y)$ may then be represented by a matrix **A** of dimensions $n \times m = N$ whose elements are equal to 1 and 0, respectively, corresponding to the transparent and opaque elements. The object distribution inside the FOV may also be conveniently represented by a $p \times q$ array **S**, the elements of which have angular sizes governed by the angle subtended by one mask element at the detector (in each direction, $\Delta\alpha \approx \text{arctg}(L/H)$, where L is the linear size of a mask element and H the mask-detector separation). These angular dimensions define the geometric (or intrinsic) angular resolution of the instrument. The convolution expressed in Equation (2.1) may then be rewritten in the form of a discrete correlation:

$$D_{jk} = \sum_l \sum_i A_{j+l,\,k+i} S_{li} + B_{jk}\,, \tag{2.3}$$

where the summations should be extended to infinity, even if they are limited by the physical dimensions of the detector and of the aperture **A**. Practically the summations are extended up to the limits of the FOV, where the incoming fluxes are completely uncoded and the corresponding contribution to each detector pixel can therefore be included into the background term.

The encoding procedure expressed by Equation (2.3) may also be expressed in terms of a system of linear equations:

$$\mathbf{d} = \mathbf{Ws} + \mathbf{b}\,, \tag{2.4}$$

where the vectors **d** and **s** are obtained by lexicographic reordering of the matrices **D** and **S**, respectively, and the matrix **W** has the block Toepliz form generated by packing the array **A**, as described by Andrews and Hunt (1977, Chapter 3). The elements of the matrix **A** are arranged in the array in such a way that each column k of **W** is the one-dimensional array representation of the coding pattern (working zone) associated with the kth element of the object **s**, and each row j specifies which entries of **s** contribute to the counts in pixel d_j of the detector. The **W** matrix is also referred to as a 'weighing design' (Sloane and Harwit, 1976). In this formulation the dimensions $u \times v$ of the matrix **W** depend on which zone of the FOV is considered, once the detector/mask arrangement is fixed. For example, for a telescope with a replicated (mosaiced) mask in which the detector is represented by a $p \times q$ array and the aperture **A** by a $(2p - 1, 2q - 1)$ array the FCFV itself is automatically defined as a $p \times q$ array and the **W** matrix is square with dimensions $(2p - 1, 2q - 1)$. In the case of a single cycle mask of the same size as the detector if we want to deal with a square **W**, the array **S** must include a part of the PCFV. Figure 2.4 gives examples of square weighing designs **W** in both the above cases.

2.2. Direct deconvolution methods

Among the several possible deconvolution techniques, in this section we shall confine ourselves to describing the methods that can be derived directly from the image formation models expressed by Equations (2.1), (2.2), and (2.4).

First of all we point out that a straightforward way of performing the image recon-

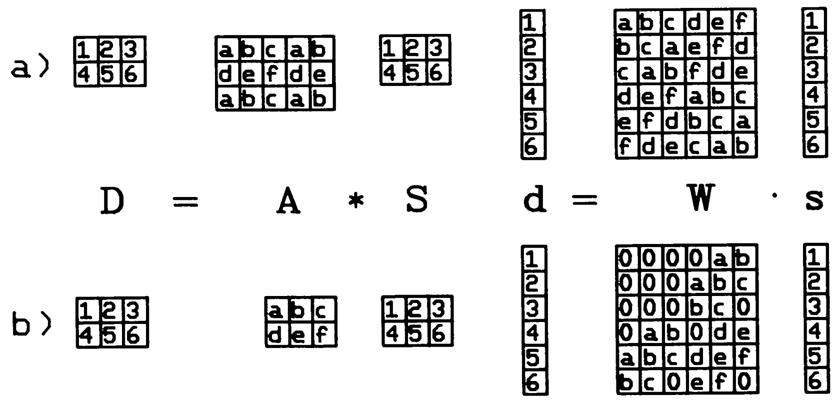

Fig. 2.4. An example of a square Weighing matrix associated with two different mask-PSD configurations: (a) A 2 × 2 (minus one row and one column) mosaic arrangement; the W matrix represents only the FCFV. (b) Mask and detector of the same dimensions. The **W**-matrix represents the FCFV plus a part of the PCFV. The O's in the **W**-matrix indicate that a shielded instrument is being considered, hence no contribution to the shadowgram is expected from photons not intercepting the mask.

struction (Equation (2.2)) is by means of the Fourier transform, which reduces a convolution to a simple multiplication. Providing the Fourier transform of each function exists, the estimate $\hat{S}$ is then given by:

$$\hat{S} = F^{-1}(F(D)/F(A)) = S + F^{-1}(F(B)/F(A)), \tag{2.5}$$

where F and F^{-1} are the Fourier-transform operator and its inverse, respectively. In the discrete formulation the second term is a matrix whose elements are obtained by dividing each entry of the Discrete Fourier Transforms (DFT) of the array $\mathbf{D}(F_d(\mathbf{D}))$ by the corresponding one in $F_d(\mathbf{A})$ (Andrews and Hunt, 1977, Chapter 7). In practice the implementation of this technique by means of DFT algorithms can produce noise amplification due to small values in $F_d(\mathbf{A})$. In this case the distortion and deterioration of the reconstructed image becomes dramatic even in relatively high signal to noise ratio situations ($\lesssim 100$). The presence of small or null terms in $F_d(\mathbf{A})$ appears to be a quite general property of binary matrices (i.e., with entries only 0 or 1), thus rendering the direct Fourier deconvolution unsuitable as a general deconvolution method.

Another method of decoding is suggested by Equation (2.2), which can be rewritten in the discrete case in the form of a cross-correlation with a matrix **G**:

$$\hat{S}_{jk} = \sum_l \sum_i G_{j+l,k+i} D_{li} = G * A * S + G * B \tag{2.6}$$

The choice of the decoding matrix **G** must be such that **G** ∗ **A** is as close as possible to a delta function, in order to preserve the object features within the system resolution. One method is to use the array **A** itself as the decoding matrix in Equation (2.6) which is similar to a backprojection.

Other forms of this algorithm are based on a decoding array derived from **A**, for instance, in the following manner:

$$\begin{cases} G_{jk} = 1\,, & \text{if} \quad A_{jk} = 1\,, \\ G_{jk} = \tau/(\tau - 1)\,, & \text{if} \quad A_{jk} = 0\,, \end{cases} \tag{2.7a}$$

where $\tau = M/N$ is the overall transparency of the basic mask pattern. In this way, the sum of the **G** elements being equal to zero, any d.c. background is automatically removed from the reconstructed image (Fenimore and Cannon, 1978). A different choice for **G** can be:

$$\begin{cases} G_{jk} = 1\,, & \text{if} \quad A_{jk} = 1\,, \\ G_{jk} = -\lambda/(M-\lambda)\,, & \text{if} \quad A_{jk} = 0\,, \end{cases} \tag{2.7b}$$

where λ again depends on the transparency of the mask, being equal to the average height of the sidelobes in the autocorrelation function (see Section 2.3 and Fenimore, 1978). The use of this definition of **G** leads to the total number of counts in the image (FCFV only) being equal to the counts detected, while under Equation (2.7a) the integrated count is zero. Decoding with either these arrays is termed 'balanced correlation' due to the different weights (w) given to the opaque elements.

The formalism adopted in Equation (2.4) suggests an alternative method for the deconvolution of the shadowgram **D**. If the **W** matrix is square we can reconstruct the image by using its inverse:

$$\hat{\mathbf{s}} = \mathbf{W}^{-1}\mathbf{d} = \mathbf{s} + \mathbf{W}^{-1}\mathbf{b}\,. \tag{2.8}$$

This obviously requires that the mask pattern originates a non-singular matrix. The existence of $\mathbf{W}^{-1}$ is of course connected with the non-ambiguity of the mask pattern: each working zone must be different (i.e., the rows of **W** must be mutually independent). When the $\mathbf{W}^{-1}$ matrix exists, a perfect reconstruction of the object is guaranteed by the inversion method, but, as with Fourier deconvolution, the noise contribution $\mathbf{W}^{-1}\mathbf{b}$ can dominate the reconstructed image. This problem occurs when **W** is nearly singular (ill-conditioned) producing large entries in the inverse $\mathbf{W}^{-1}$. The near-singularity of the **W** matrix will occur if the aperture **A** produces some rows in **W** which are approximately linear combinations of others, and is a frequent characteristic of linear imaging systems. For the sake of completeness we can add that if **W** is singular or not square it is still possible to define a solution of the linear system (2.4) by use of the so-called 'generalized inverse' (Penrose, 1955; Fisher, 1967; Pratt, 1978, Chapter 8) and related numerical algorithms (Andrews and Hunt, 1977, Chapter 8; Pratt, 1978, Chapter 14). These numerical filters, such as the Singular Value Decomposition (SVD) (Huang and Narendra, 1975; Pratt, 1978, Chapter 5; Maeda and Murata, 1984) are also useful in solving the general problem of ill-conditioning in matrix inversion.

In Figure 2.5 is shown a comparison between the image of a point source, in a uniform background distribution, obtained by the inversion method and by balanced correlation. The degradation of the image decoded by inversion is evident when compared to the results of the correlation algorithm.

It is worthwhile to point out that the correlation process (Equation (2.6)) can be expressed in the form of a linear system of equations by applying to the **G** matrix the same reordering method used to construct **W** from the mask pattern. The bidimensional estimate $\hat{\mathbf{S}}$ is then derived by folding the vector $\hat{\mathbf{s}}$ obtained from

$$\hat{\mathbf{s}} = \overline{\mathbf{W}}\mathbf{d} = \overline{\mathbf{W}}\mathbf{W}\mathbf{s} + \overline{\mathbf{W}}\mathbf{W}\mathbf{b}\,, \tag{2.9}$$

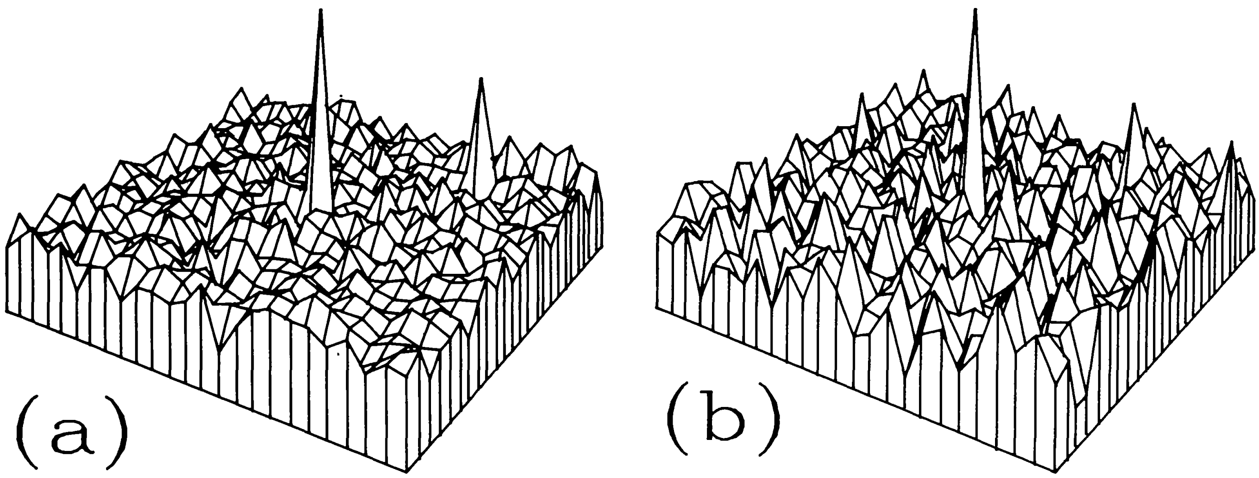

Fig. 2.5. Images of two point sources superimposed on a uniform background, obtained with a random mask (basic pattern 25 × 25) using the following decoding processes: (a) balanced correlation; (b) Matrix inversion (inverse filter). From the picture the image degradation in case (b) is well evident with respect to (a), in particular the lower intensity source almost disappears in the background structure.

where $\overline{\mathbf{W}}$ is still a $(p \times q,\ p \times q)$ array containing the **G** elements re-ordered in the lexicographic way. For example, in the case of balanced correlation $\overline{\mathbf{W}}$ takes the form $(1 + w)\mathbf{W}^T - w\mathbf{U}$, where **U** is a matrix with all elements equal to 1 (unit matrix). This allows the two methods (correlation and inversion) to be discussed in the same formalism as far as the study of the performance of mask systems is concerned (Caroli *et al.*, 1984). In the following discussion about optimum mask designs and system configuration, we will implicitly assume that the decoding is performed in one of these two manners.

2.3. System Point Spread Function and Modulation Transfer Function

As seen previously, the result of the object reconstruction depends on both the mask pattern **A** and of the decoding array **G**. The quality of any such choice can be evaluated by studying the System Point Spread Function (SPSF), defined as the reconstructed image of a point source:

$$\mathrm{SPSF} = \mathbf{G} * \mathbf{A} = \overline{\mathbf{W}}\mathbf{W} \tag{2.10}$$

In the case of decoding by the inverse matrix method ($\overline{\mathbf{W}} = \mathbf{W}^{-1}$), the SPSF is a delta function and so the object reconstruction is perfect. However, as already said, the inverse matrix can be ill-conditioned producing an amplification of the noise term that can produce distortion and deterioration in the reconstructed image.

The correlation method does not suffer from this problem, because the matrix always has finite elements. For example, in the case of autocorrelation the elements of $\overline{\mathbf{W}}$ are 0 or 1 and in the case of balanced correlations ($\overline{\mathbf{W}} = (1 + w)\mathbf{W}^T - w\mathbf{U}$) the absolute value of the elements is always 1 or $|w|$. On the other hand, using the correlation method, the SPSF is no longer in general a delta function and a point in the object **S** will contribute to the reconstructed image with a distribution extended over a number of different elements. Therefore, the SPSF consists of, in addition to the peak corresponding to the source element in **S**, a series of spurious lobes which cause the presence of artifacts. This degradation in the decoded image, depending on the structure of the SPSF and not on the statistical quality of the data, cannot be reduced by increasing the exposure time. In the case that the object S is not point-like, but complex (several point sources, extended source) the image can be further deteriorated because the sidelobes associated with every source induce a cross-talk between different elements. This results in the superposition of a signal-dependent noise connected with the structure of the object itself, severely limiting the possibility of finding weak sources or resolving structures (Fenimore and Cannon, 1978). In Figure 2.6(a) and (b) the SPSF is shown for a 50% transparent random mask pattern for both auto- and balanced correlation as defined by Equation (2.7a). It can be seen that for the case of balanced correlation the mean value of the sidelobes is zero. In the following sections we will often refer to the Autocorrelation Function (ACF) $\mathbf{A} * \mathbf{A}$ to study the mask patterns because this function depends only on their intrinsic characteristics. Furthermore, for aperture designs consisting of mosaiced mask patterns the appropriate ACF to study is cyclic in nature, i.e.:

$$(\mathbf{A} * \mathbf{A})_{jk} = a_{jk} = \sum_{1}^{n}{}_{l} \sum_{1}^{m}{}_{i} A_{li} A_{uv} ;$$
$$u = (j + 1) (\mathrm{mod}\, n) , \quad v = (k + i) (\mathrm{mod}\, m) . \tag{2.11}$$

Unless specified otherwise we will, henceforth, assume all ACF's to be cyclic.

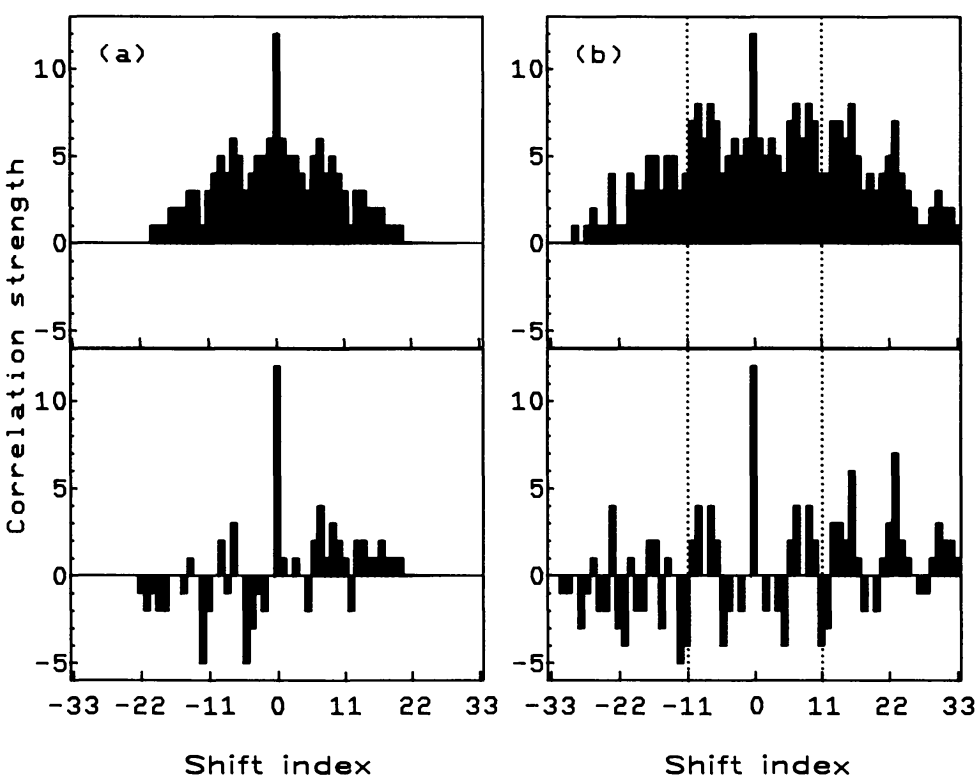

Fig. 2.6. The System Point Spread Function (SPSF) of a monodimensional random sequence of length 32 (50% open): (a) Non-Cyclic auto- (*upper*) and balanced- (*lower*) correlation. (b) Cyclic auto- (*upper*) and balanced- (*lower*) correlation. The dotted lines indicate the limit of the FCFV. The SPSF in this region is symmetric.

The Modulation Transfer Function (MTF) is another characteristic function which can provide information about the imaging capability of an instrument. For coded aperture systems it is defined as:

$$\mathrm{MTF} = F_d(\mathbf{G} * \mathbf{A}) = F_d(\mathbf{G})F_d(\mathbf{A})\,. \tag{2.12}$$

The MTF, therefore, is equivalent to the SPSF expressed in the spatial frequency domain and, as such, indicates the relative transmission strengths of sampled spatial frequencies. In the ideal case all the sampled frequencies will be transmitted with equal intensity, resulting in a flat (monovalued) MTF, whilst in the real case the presence of very low or zero values and/or large variations in the function leads to a degraded reconstructed image. In order to avoid this situation the mask pattern **A** and the decoding function **G** must be chosen so as to provide a frequency response as flat as possible. It can be shown that the optimal frequency response of a mask **A** depends only on its pattern, while the shape and the dimension of its elements affect other characteristics of the reconstructed image, for instance the geometric angular resolution and the signal to noise ratio (Fenimore, 1980). This function is very useful in evaluating the performance of a real instrument because it allows the easy introduction of physical effects such as diffraction induced by the material of the mask ($R(x, y)$) and the finite resolution of the detector $Q(x, y)$ giving:

$$\mathrm{MTF} = F_d(\mathbf{G} * \mathbf{Q} * \mathbf{R} * \mathbf{A}) = F_d(\mathbf{G})F_d(\mathbf{Q})F_d(\mathbf{R})F_d(\mathbf{A})\,. \tag{2.13}$$

2.4. Signal-to-noise ratio

The performance of an imaging telescope depends on its ability to reconstruct faithfully the fluxes from the field of view both in terms of intensity and angular distribution. One parameter which may be employed to define the quality of an instrument is the Signal-to-Noise Ratio (SNR) which determines the minimum source strength that may be detected. In an image the theoretical SNR for a particular pixel is the ratio between the expected value of intensity in that pixel and a noise term σ_{jk}:

$$\mathrm{SNR} = S_{jk}/\sigma_{jk}\,. \tag{2.14a}$$

In each pixel of the reconstructed image the noise term is defined as:

$$\sigma_{jk}^2 = \sigma_{jk}^2(S_{jk}) + \sigma_{jk}^2(\mathbf{S}) + \sigma_{jk}^2(\mathbf{B})\,, \tag{2.14b}$$

where $\sigma_{jk}^2(S_{jk})$ is the variance associated with statistical fluctuations of the flux in the (j, k)th direction, $\sigma_{jk}^2(\mathbf{B})$ is the variance due to the total background noise, and $\sigma_{jk}^2(\mathbf{S})$ is the variance contributed by all the other object elements in the FOV. The last term arises from both statistical fluctuations of the fluxes and systematic effects, if any, induced by the SPSF sidelobe structure on the different source elements S_{jk} (cross-talk).

In the case of decoding by inversion of the weighing matrix **W** or by correlation, it is possible to obtain an analytical expression for the expected SNR in the reconstructed pixels by considering that the statistics of the fluxes and background are Poissonian and without presupposing the type of mask pattern. For the inversion method, it can be demonstrated (Sloane *et al.*, 1969; Harwit and Sloane, 1979, Chapter 3) that the variance in each pixel is weighted by the sum of the squares of the inverse matrix elements. In the case of a replicated mask, each row and column of **W** being a cyclic permutation of the same sequence, the contribution $\sigma_{jk}^2(\mathbf{B})$ is uniform over the reconstructed image. The mean variance (or mean-square error) of the reconstructed image ($\sigma^2 = \Sigma_{jk}\,\sigma_{jk}^2/N$) is:

$$\sigma^2 = (S_{\text{tot}} + B_{\text{tot}})\tau^2\,\text{Trace}(\mathbf{W}\mathbf{W}^T)^{-1}\,, \tag{2.15}$$

where S_{tot} and B_{tot} represent the integrated source and background counts, respectively, and $\tau = M/N$ the open fraction of the mask. From Equation (2.15) the mean variance is proportional to $S_{\text{tot}} + B_{\text{tot}}$ which is the variance in the total number of counts in a simple counting system with the same active area. Also, Equation (2.15) indicates that the SNR is, on the average, not affected by systematic contributions from the object structure, but depends on the mask pattern characteristics.

Applying the same analysis to the correlation method it is possible to show that in this case the variance in each reconstructed pixel is the sum of a uniform statistical contribution from the fluxes and background, and an object dependent term that is proportional to the square of the flux intensities (Caroli *et al.*, 1984). The expression for the mean variance is then:

$$\sigma^2 = \frac{1}{N}\sum_j\left(\sum_k(a_{jk} - M\delta_{jk})S_{jk}\right)^2 + \frac{\tau}{1-\tau}(S_{\text{tot}} + B_{\text{tot}}) \tag{2.16}$$

where δ_{jk} is the Kronecker delta. The first term is the systematic contribution dependent on the SPSF sidelobes, a_{jk} being the values of the autocorrelation matrix $\mathbf{A} * \mathbf{A}$ in the lexicographic reordered form. The second term arises from statistical fluctuations and is again proportional to the total counts. The only characteristic of the mask pattern that influences this factor is the ratio of transparent to opaque elements $\tau/(1-\tau)$.

Both the above expressions for the average noise term depend explicitly on the mask transparency. Fenimore (1978) and Skinner (1984) have studied how this parameter affects the reconstructed SNR with a view to optimizing the aperture design with respect to a wide range of observational conditions (number of sources, source intensities, background count rate). On a basis of purely statistical considerations, without taking into account any systematic effects, they have shown that in the typical conditions of high energy astronomy (few point sources, high background) the optimum transparency is very close to 50%. Furthermore the loss in SNR occurred by the use of a mask transparency of 50% instead of the optimum open fraction is always less than 30% (Figure 2.7).

Care must be taken in interpreting the SNR in terms of significance. In coded mask systems it must be remembered that the observation of each element in the FOV consists of a number of simultaneous measurements of flux and background, the exact number depending on the corresponding working zone of the mask pattern. The larger the number of measurements, the more likely a certain value of sigma will be exceeded by

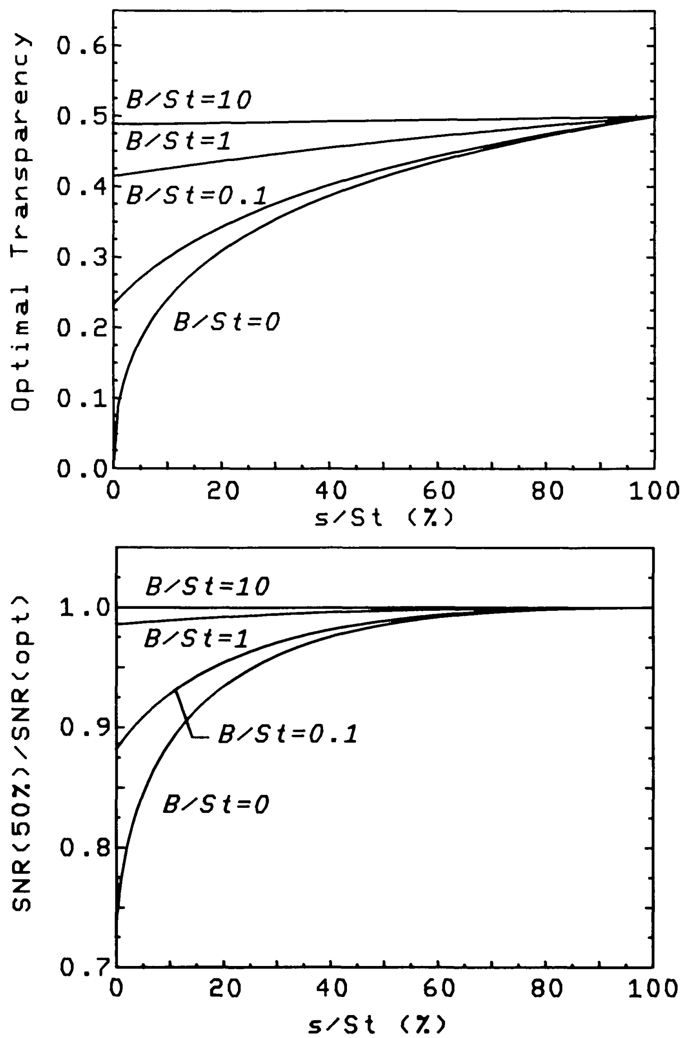

Fig. 2.7. (a) Optimum mask transparency as a function of (S/St) where S and St are a single point source contribution and the sum of all fluxes in the field of view, respectively, for different values of B/St, where B is the background per pixel. (b) The ratio between the SNR achieved by using a mask of 50% transparency to that resulting from the use of a mask of optimum transmission under the same conditions. (Fenimore, 1978).

chance, therefore, in the case of no *a priori* knowledge of source positions, the significance of a particular detected peak will be less. Figure 2.8 shows how the values of observed sigma have to increase as the number of measurements (pixels) in order to retain the same significance, assuming the counting rates in each pixel are mutually independent (i.e., no systematic effect in the reconstructed pixels) (Gunson and Polychronopulos, 1976).

3. Coded Aperture Mask Designs

Since the first proposal by Mertz and Young (1961) to use coded apertures for imaging in the high-energy spectral range, a large number of mask designs have been conceived and employed with a view to optimizing the quality of the images produced. Although

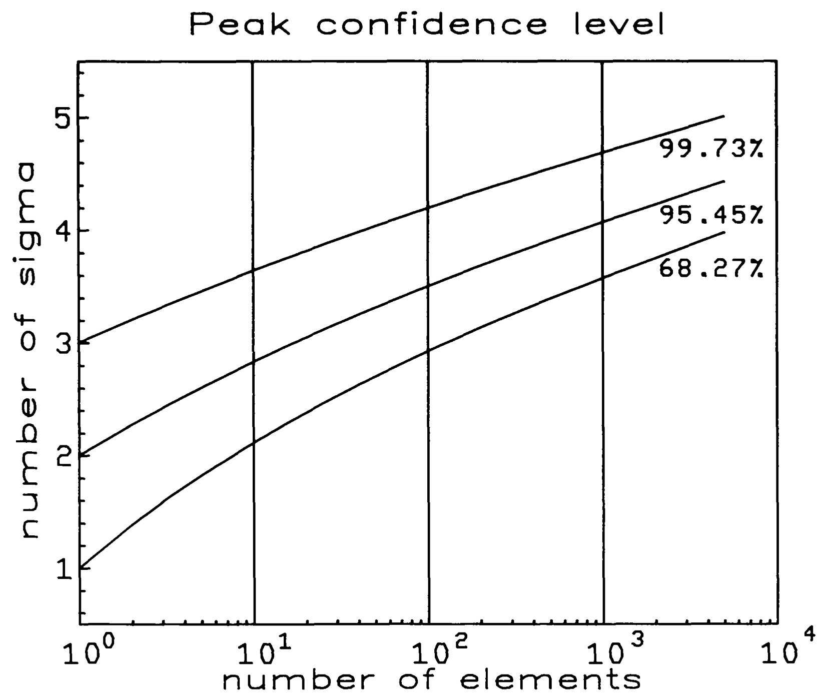

Fig. 2.8. The variation in confidence level for a particular SNR as a function of the number of mask elements, in order to retain the same significance (in the case of no *a priori* knowledge of source positions).

the application of advanced numerical techniques for deconvolution and restoration (Daniell, 1984; Willingale *et al.*, 1984) can greatly enhance the quality of images derived even from quite poor data sets, these methods are always very time consuming and require large amounts of computing power. On the other hand, relatively simple and fast methods of image reconstruction may be employed if the instrument design, in particular the choice of the mask pattern, has been sufficiently well studied.

3.1. Fresnel Zone Plates and Random Pinhole Masks

The very first type of coded aperture proposed in the early days of multiplex imaging was the Fresnel Zone Plate (FZP) (Mertz and Young, 1961). Even though this type of coded aperture has not found a place in high-energy astronomy it was implemented successfully for example in X- and γ-ray tomographic imaging (Ceglio *et al.*, 1977, Laub and Reinhardt, 1983). The Fresnel Zone Plate (FZP) (Barrett and Horrigan, 1973; Barrett and DeMeester, 1974) in theory consists of a circularly-symmetric aperture with a transmission function proportional to the cosine of the square of the distance from the centre: i.e.,

$$A(r) \sim \cos r^2 ; \quad 0 \leq r \leq +\infty . \tag{3.1}$$

In practice, as a continuously variable transmision is impossible to achieve for anything other than one energy, the aperture has to be approximated by a series of concentric annuli which are alternately opaque and transparent, with the radius of the nth annulus being given by

$$r_n = r_0 \sqrt{n} , \tag{3.2}$$

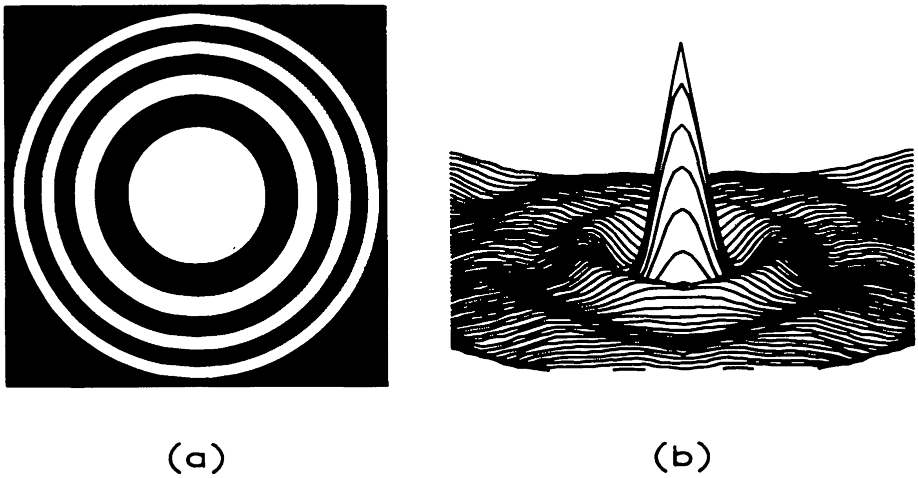

Fig. 3.1. (a) A Fresnel Zone Plate (FZP) pattern with three opaque rings and (b) its autocorrelation function.

where r_0 is the radius of the central disk which may be either opaque or transparent. Figure 3.1(a) illustrates such a pattern, which has the property that each annulus has the same area, with a resulting overall transmission of $\approx 50\%$. In the ideal case the FZP has an autocorrelation function consisting of a single peak on an otherwise flat background and it then, as described in Section 2.2, possesses optimum imaging characteristics. In practice, however, the discretized transmission function, in addition to the use of a finite sized aperture produces a poorer point spread function, exhibiting a central peak surrounded by a series of concentric lobes as shown in Figure 3.1(b). These lobes may be reduced by suitable filtering techniques (Woods *et al.*, 1975). Strictly related to the FZP is a variety of proposed coded apertures which has been discussed by Barrett *et al.* (1974).

Greater use has been made of aperture arrays based on multiple pinholes in an otherwise opaque plate. Dicke (1968) and Ables (1968) independently proposed, for use in X- and γ-ray astronomy, apertures consisting of a large number of randomly spaced pinholes having an overall transmission $\approx 50\%$. In principle this is a logical extension of the simple pinhole camera, which itself has since been used successfully in the astronomical context (Holt, 1976), and Section 5.4). The imaging properties of the pinhole camera are ideal, the autocorrelation being a delta-like function, but it suffers greatly from a conflict between resolution and sensitivity. The angular resolution is proportional to the hole size, so for fine resolution a small hole is essential. The sensitivity, however, is determined by the amount of flux detected, thus a large hole would be required. These two conditions are clearly incompatible. The idea behind the random array is that the transmission and, hence, the sensitivity, may be increased proportionally to the number of pinholes, whilst retaining the angular resolution commensurate with the size of each hole. Random patterns do not place any constraint on the dimensions of the aperture nor on its overall transparency. In particular, masks of dimensions $2^n \times 2^n$ elements may be employed, allowing image reconstruction by means of Fast Fourier Transform (FFT) algorithms. As in the case of the FZP, however, their

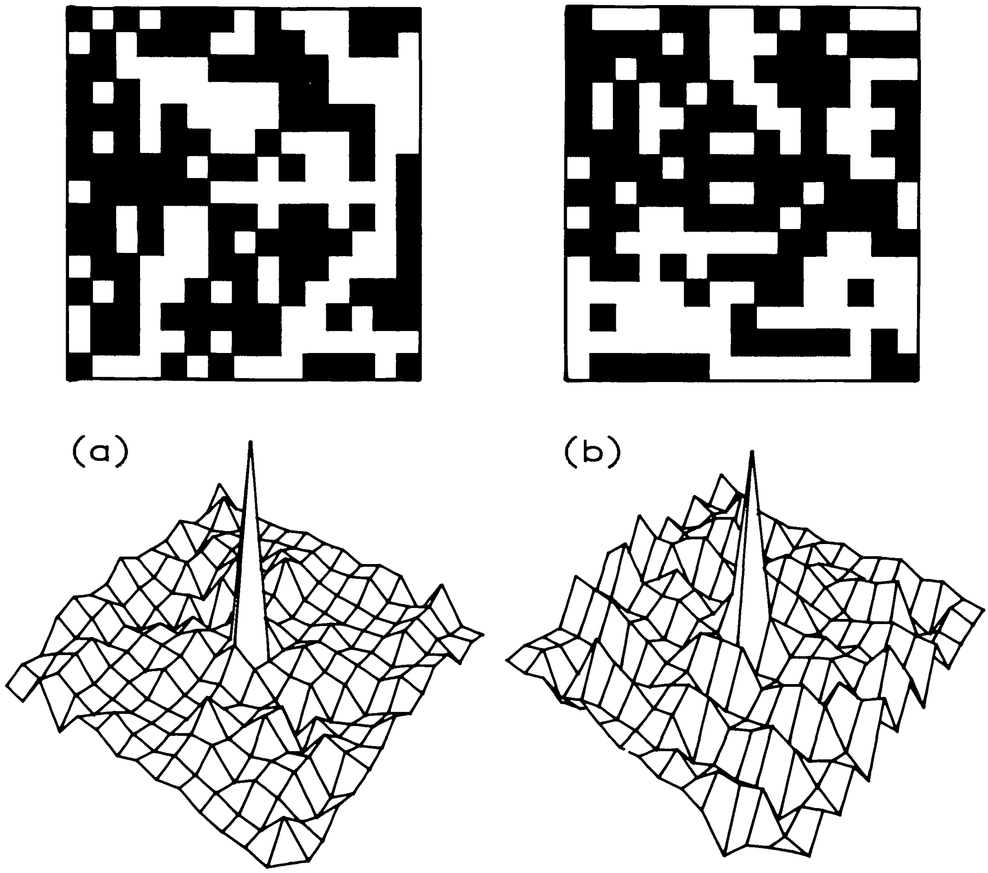

Fig. 3.2. Two 15 × 15 random masks of 50% transparency. Their different inherent noise characteristics are reflected in their different autocorrelation functions (*below*). Decoding by correlation the variance induced by the sidelobe structure in reconstructed images from mask (b) is about twice that for mask (a), while the variance for **W** inversion is ≈3 times higher due to the noise amplification factor Trace $(\mathbf{WW}^T)^{-1}$.

use is limited by the non-ideal nature of their imaging capabilities. In fact the autocorrelation of a random array consists of a large central peak surrounded by pronounced side lobe structures. Imaging of many point sources or of extended sources can cause these sidelobes to produce spurious peaks in the background, or if matrix inversion decoding is employed noise amplification may occur. On the other hand it is possible (Caroli *et al.*, 1984), once the mask dimensions are fixed, to choose the pattern arrangement by minimizing the sidelobe structure of the ACF and/or the Trace$(\mathbf{WW}^T)^{-1}$. Figure 3.2 shows the autocorrelation function of two random patterns with equal dimensions and the same open fraction, but with different inherent noise structures.

3.2. Non- and uniformly-redundant arrays

Golay (1971) proposed a class of coded aperture designs which have nearly perfect imaging characteristics, known as non-redundant arrays (NRA's). The basis upon which they are constructed is that the vector separation between any two holes must occur once, and once only throughout the entire mask. The autocorrelation of these arrays is then a single peak, of value equal to the number of pinholes, with no sidelobes up to a certain lag δ (where the maximum distance between any two holes is 2δ).

Thereafter the autocorrelation fluctuates between 1 and 0. So if the linear extension of the object S is less than δ the reconstructed image is perfect with at most a d.c. term superimposed, while if S is larger then artifacts are present due to the fluctuations in the autocorrelation function. This implies that if it is required to have a large FOV without loss of angular resolution then it is necessary to increase dramatically the physical dimensions of the mask. Furthermore, this kind of mask is subject to a severe limitation on the number M of transparent elements: typically the open fraction of NRA's ranges from $\approx 10\%$ to $\approx 1\%$ for $10^2 < M < 10^4$. Therefore, even in the absence of noise, the sensitivity of such a system is strongly affected. For these reasons the NRA's have not found use in high energy astronomy, instead applications have been attempted in nuclear medicine (Chang *et al.*, 1975; Fleming and Goddard, 1984) and in optical and infrared astronomy (Brown, 1978; Aitken *et al.*, 1981).

By contrast a class of arrays which has been very successful in X- and γ-ray astronomy is that based on cyclic difference sets (Baumert, 1969). A cyclic difference set $\Delta(N, M, \lambda)$ is a sequence of M residues, modulus N, such that for any residue $\rho \neq 0 (\bmod N)$ the congruence:

$$\delta_i - \delta_j \equiv \rho (\bmod N)$$

admits λ solution pairs (δ_i, δ_j) with δ_j and δ_i in Δ. To each difference set it is possible to associate a binary sequence $\{\alpha_i\}$ of length N, wherein α_i takes the value 1 if i belongs to Δ and 0 otherwise. The (cyclic) autocorrelation function of this binary sequence is then always of the form (Baumert, 1971, Chapter 1):

$$a_i = \sum_0^{N-1}{}_j \, \alpha_j \alpha_k$$

$$= \begin{cases} M, & \text{if } \; j = 0 (\bmod N), \\ \lambda = M(M-1)/(N-1), & \text{if } \; j \neq 0 (\bmod N), \end{cases} \quad k = (j+i)(\bmod N); \tag{3.3}$$

i.e., a single peak on a perfectly flat background. Furthermore, several methods exist for packing these mono-dimensional sequences into bi-dimensional arrays whose autocorrelation functions have the same attributes. The autocorrelation function has only two values – one associated with the peak and the other with the flat sidelobe structure – as a consequence of the constant number of times (λ) the vector spacing between a pair of 1's occurs regardless of that spacing (up to a certain limit). For this reason these arrays are also called Uniformly Redundant Arrays (URA's) (Fenimore and Cannon, 1978). In this formulation, it is possible to regard the NRA's as a subclass of URA's in which $\lambda = 1$ (and which are derived from the so-called planar difference sets).

Among the Cyclic Difference Sets there are two subclasses which are particularly suitable for generating masks for multiplex imaging:

(a) Singer sets (Singer, 1938; Baumert, 1971, Chapter 5): these sets are characterized by the parameters $N = (t^{m+1} - 1)/(t - 1)$, $M = (t^m - 1)/(t - 1)$, and $\lambda = (t^{m-1} - 1)/(t - 1)$, where t is a prime number.

(b) Hadamard sets: the characteristic parameters in this case take the form

$N = 4t - 1$, $M = 2t - 1$, $\lambda = t - 1$ with t being an integer. The name of these sets is derived from their connection with Hadamard matrices (Hall, 1967; Baumert, 1971, Chapter 4). The known Hadamard sets may be classified not only by the value of N, but also by their construction method of which at least three are known:

(1) Quadratic residues. If N is prime, the set is given by the residuals, (mod N), of the squares of the first $(N + 1)/2$ integers.

(2) Twin primes. These sets are classified by $N = p \times q$ where p and q are both prime and $|p - q| = 2$.

(3) Sets where N takes the value $2^m - 1$ and m is an integer > 1. In fact these sets are complementary to the Singer sets with $t = 2$. The characteristic binary sequences in this case are known as pseudo-noise (PN) or m-sequences (MacWilliams and Sloane, 1976).

Once the binary sequence has been generated, if its length N can be factorised into a product of two integers ($N = p \times q$) it is possible to form a two-dimensional array. The simplest method is to order the N elements by rows or columns into the desired array (Figure 3.3(a)), while a more complicated solution is to order along the extended diagonal (Figure 3.3(b)), although this requires the further limitation that p and q must be mutually prime.

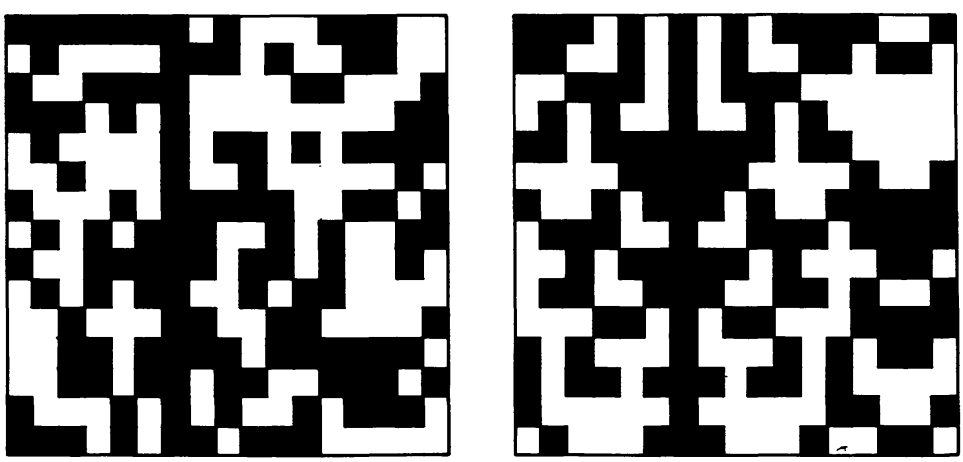

(a) (b)

Fig. 3.3. (a) A 255 element Hadamard sequence folded by rows into a 15 × 17 two-dimensional array. (b) The same sequence folded along the extended diagonal: starting at the top left hand square, the series is written down the main diagonal continuing at the opposite side when an edge is reached.

Fenimore and Cannon (1978) have proposed another method for constructing a two-dimensional mask in the Twin Prime case, avoiding the generation of the length N binary sequence. The 2-D mask pattern (Figure 3.4) is generated from two quadratic residues sequences ($\{\alpha_i\}$, $\{\beta_i\}$), of order p and q, respectively, according to the following

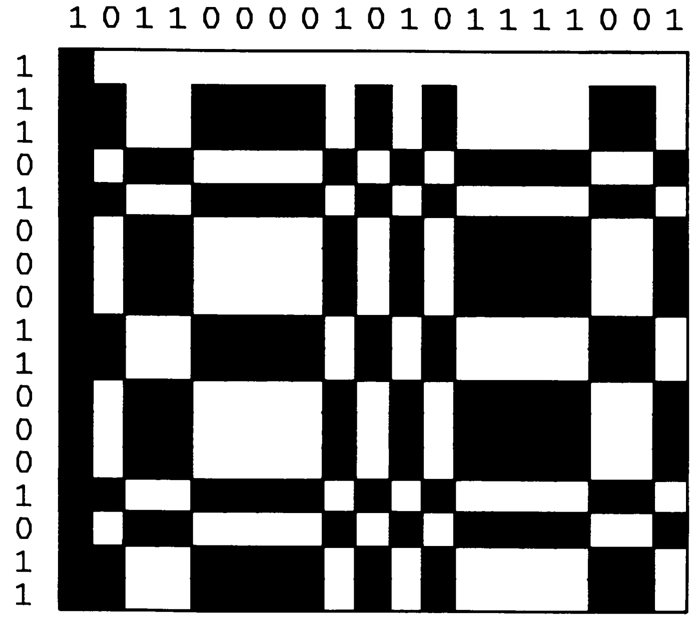

Fig. 3.4. A Fenimore and Cannon 17 × 19 twin prime array with its two generating one-dimensional pseudo-random sequencies.

rules:

$$\begin{cases} A_{j1} = 0, & i = 1, p\,, \\ A_{1k} = 1\,, & k = 2, q\,, \\ A_{jk} = \alpha_j \beta_k + (1 - \alpha_j)(1 - \beta_k)\,, & j = 2, p;\, k = 2, q;\, \alpha_j,\, \beta_k \in \{0, 1\}\,. \end{cases}$$

The result is exactly equivalent to ordering the length $N = p \times q$ twin prime sequence by the extended diagonal method. From the definition of the various difference sets, it can be seen that whereas the Hadamard masks must have a transparency of almost 50%, those based on Singer sets have a variable transmission depending inversely on the value of t ($M/N \approx 1/t$).

As these mask designs have all been discussed in terms of a cyclic autocorrelation function, they are perfectly suited for use in the 2×2 mosaic form as discussed in Section 2. However, the manner in which the mosaic is constructed depends on the type of folding (i.e., by rows or extended diagonal) which is employed. The general criterion which must be satisfied is that every working zone corresponding to a point source in the fully coded FOV must contain a complete, although permutated, mask pattern (Figure 3.5). From this criterion, it follows immediately that, as each row in the weighing design **W** of a replicated URA is a cyclic permutation of the basic pattern sequence, **W** satisfies the following relation:

$$\mathbf{W}^T\mathbf{W} = \mathbf{W}\mathbf{W}^T = (M - \lambda)\mathbf{I} + \lambda\mathbf{U}\,, \tag{3.4}$$

where **I** and **U** are the identity and unit matrices, respectively.

Using Equation (3.4) it is possible to demonstrate another useful property of NRA

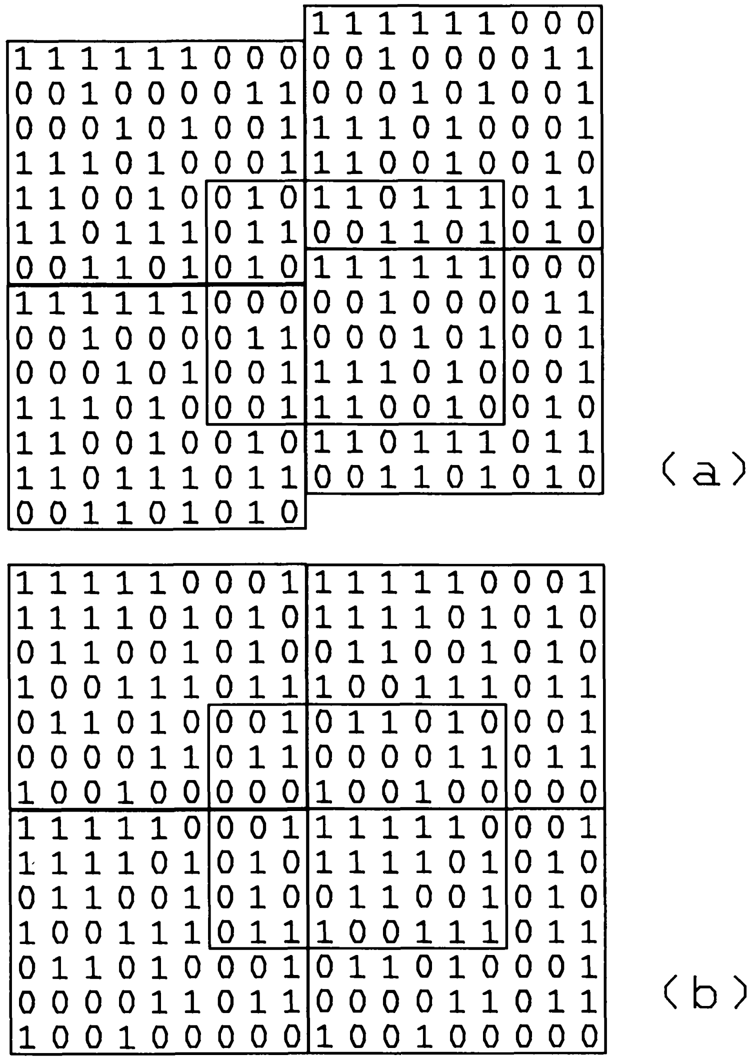

Fig. 3.5. (a) A 2 × 2 mosaic of a basic pattern folded by rows. (b) A similar mosaic of a basic pattern ordered along the extended diagonal. Each working zone (e.g., that outlined in each diagram) contains a complete, though cyclically permutated basic mask pattern. Removing one row and one column it is guaranteed that each working zone is a different permutation.

and replicated URA masks: the inverse of $\mathbf{W}$ may be analytically constructed, and is simply proportional to the transpose of $\mathbf{W}$ (Baumert, 1971, Chapter 2; Miyamoto, 1977; Harwitt and Sloane, 1979, Chapter 3):

$$\mathbf{W}^{-1} = \frac{1}{(M-\lambda)}\left(\mathbf{W}^T - \frac{\lambda}{M}\,\mathbf{U}\right). \tag{3.5}$$

The fact that the square of the $\mathbf{W}^{-1}$ entries are almost uniform ($W_{jk}^2 < 1/M^2$) means that the inversion method of decoding does not suffer from the problem of noise amplification (see Section 2) and the variance of the reconstructed pixels is almost independent from the object structure. From Equation (3.5) it can be seen that the inversion method for the case of URA's (and NRA's) is equivalent to the correlation method in the form expressed in Equation (2.9).

In the case of masks based on Hadamard sequences with $N = 2^m - 1$, a further advantage is the possibility to use the Fast Hadamard Transform (FHT) for decoding the image (Lempel, 1979; Harwitt and Sloane, 1979, Appendix A; Fenimore and Weston, 1981; Fenimore, 1983). The FHT is a very efficient algorithm which allows the reduction of the deconvolution process to a set of addition and subtraction operations, decreasing the computation time by a factor of $\approx \ln N/N$.

Until now it has been implicitly assumed that the mask patterns are based on arrays having square or rectangular elements. Recently, Finger and Prince (1985) have proposed mask designs based on Skew Hadamard sequences mapped onto an hexagonal lattice. The URA's based on these cyclic difference sets are antisymmetric with respect to the central element of the pattern. The Skew Hadamard sequences are a subset of the quadratic residues set and exist only for order $N = 4t - 1$ where N must be prime (Johnsen, 1966). In order to construct the corresponding masks, the quadratic residues binary sequence is mapped onto a 2D-lattice with axes at 60°. In particular, under the restriction that $N = 12t + 7$, it is possible to construct masks called Hexagonal URA's (HURA) that have a pattern depending on the 'periodicity parameter' η that is a solution of the equation $\eta \equiv (\eta - 1) (\mathrm{mod}\, N)$, within an overall hexagonal configuration (Figure 3.6). These may be easily implemented for use with round position sensitive detectors or circularly shaped arrays of detectors (see Section 5.6). Implicit in these mask designs is a symmetry that gives rise to a complete inversion of the pattern under a 60° rotation. This characteristic provides a useful solution for some problems generated by non-uniform background, in that a mask/anti-mask system (see Section 4.1) can easily be realized.

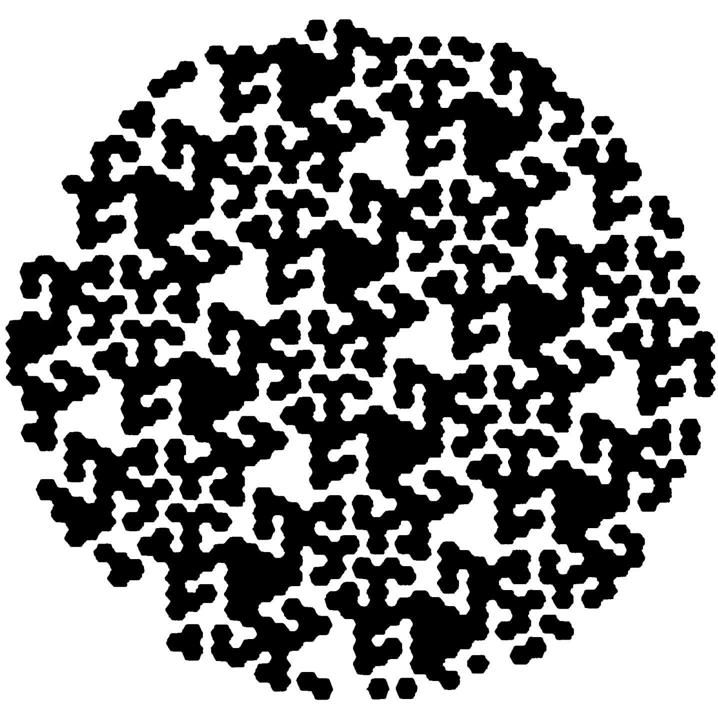

Fig. 3.6. An hexagonal URA of order 139. A 60° rotation turns the pattern into its complement: open and opaque elements are exchanged.

3.3. Pseudo-noise product and geometric masks

A limitation in the use of URA's is the fact that it is possible to map a mono-dimensional sequence onto a two-dimensional array only if its length N can be factorized into a $p \times q$ product. This means that only a limited number of the known cyclic difference sequences may be used to generate URA's, limiting the possibility of adapting an URA mask to any particular detector. To overcome this difficulty a new class of masks was recently proposed (Gottesman and Schneid, 1986) with optimum multiplexing properties. The algorithm to generate these masks consists of making the direct product of two PN sequences $(\{\alpha_j\}, \{\beta_k\})$: $A_{jk} = \alpha_j \beta_k$, for $j = 1, p$ and $k = 1, q$. The resulting arrays are referred to as a Pseudo-Noise Product (PNP) and can be implemented in any geometry $(p \times q)$ for which PN sequences exist for each dimension separately. The resulting typical patterns (Figure 3.7(a)) have the feature of being very compact and so their physical implementation is very easy and self-supporting. Since each PN sequence is 50% open, the PNP arrays typically have a transparency of 25%, therefore this design

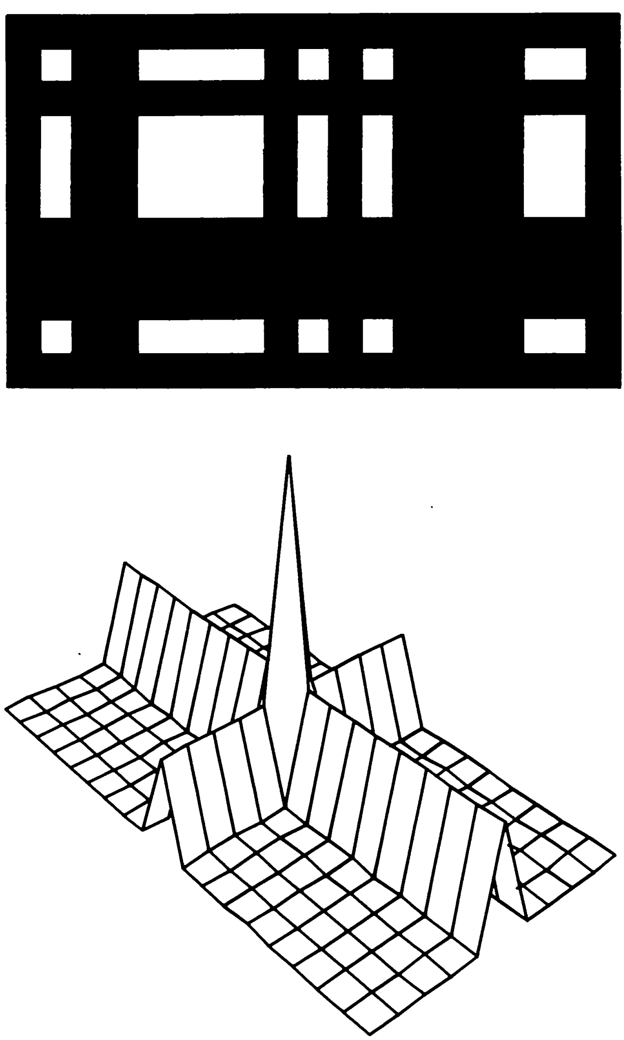

(a)

(b)

Fig. 3.7. (a) An 11×19 PNP array and (b) its (cyclic) autocorrelation function. Although sidelobe structure is present, this may be removed by a suitable definition of the decoding array (see text).

produces a loss in sensitivity (although this may be a desirable feature for medical use where sources occupy large fractions of the FOV and the background is low – see Section 2.4). In effect the cyclic autocorrelation of this mask in replicated form is not delta-like but contains a characteristic cross structure (Figure 3.7(b)). By means of a different definition of the correlation matrix it is possible to obtain a delta SPSF:

(a) For all the rows in which the entries are not all zeros:

$$G_{jk} = 1\,, \quad \text{if } A_{jk} = 1\,; \quad G_{jk} = -1, \quad \text{if } A_{jk} = 0\,.$$

(b) The opposite for all the remaining rows.

The fact that each entry of the decoding array has the same absolute value ($=1$) guarantees the complete uniformity of the variance associated to the reconstructed pixels and so complete independence from object structure.

Another type of mask with less than 50% open fraction and self-supporting patterns are the Geometric coded apertures (Gourlay and Stephen, 1983; Gourlay *et al.*, 1984).

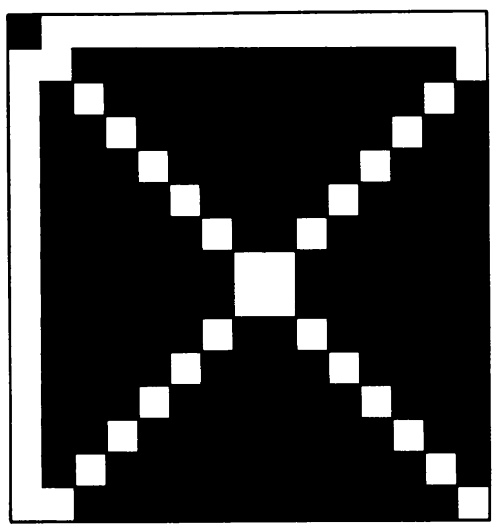

(a)

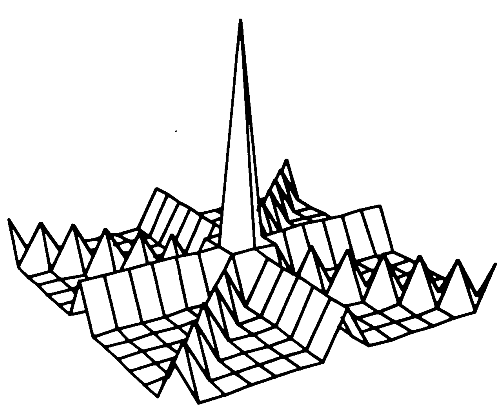

(b)

Fig. 3.8. (a) A 15 × 15 type III geometric mask design. As for the PNP arrays, the (cyclic) autocorrelation function (b) is not perfect. However, the SPSF becomes a delta-like function by defining the decoding array as follows: $G_{11} = (9n - 11 - n^2)/(n - 4)$, $G_{jk} = -3/(n - 4)$ if $A_{jk} = 0$ and $G_{jk} = 1$ otherwise (where $n \times n$ is the mask dimension and n is an odd integer).

As the name suggests, they are characterized by their geometrical regularity (see Figure 3.8(a)) and, hence, by their ease of construction. The transmission depends on the matrix dimensions, which are not restricted to the same extent as URA's. In general the mask designs are square ($n \times n$) with the severest constraint being that for one design, n must be odd. While these arrays do not enjoy an autocorrelation function with perfectly flat sidelobes (Figure 3.8(b)), again it is possible to define for all of them a simple decoding array which, in the absence of noise, allows perfect reconstruction of the field of view. However, the resulting non-uniform weights of the decoding array elements creates problems when the noise characteristics are considered. In particular, the imaging quality of the instrument is determined by the distribution of objects within the field of view. The geometric designs can be generalized in order to produce masks more flexible in shape and in openess using internal mosaicing. On the other hand this process, consisting essentially in the addition, under determined costraints, of rows and/or columns of transparent elements into the pattern, tend to produce masks which are highly ill-conditioned (Gourlay and Young, 1984).

3.4. Considerations on mask pattern performances

In order to provide a theoretical comparison between the different mask designs it is possible to analytically evaluate the response of a coded aperture telescope to a given ratio between source and background counts. Figure 3.9 shows the relative significance

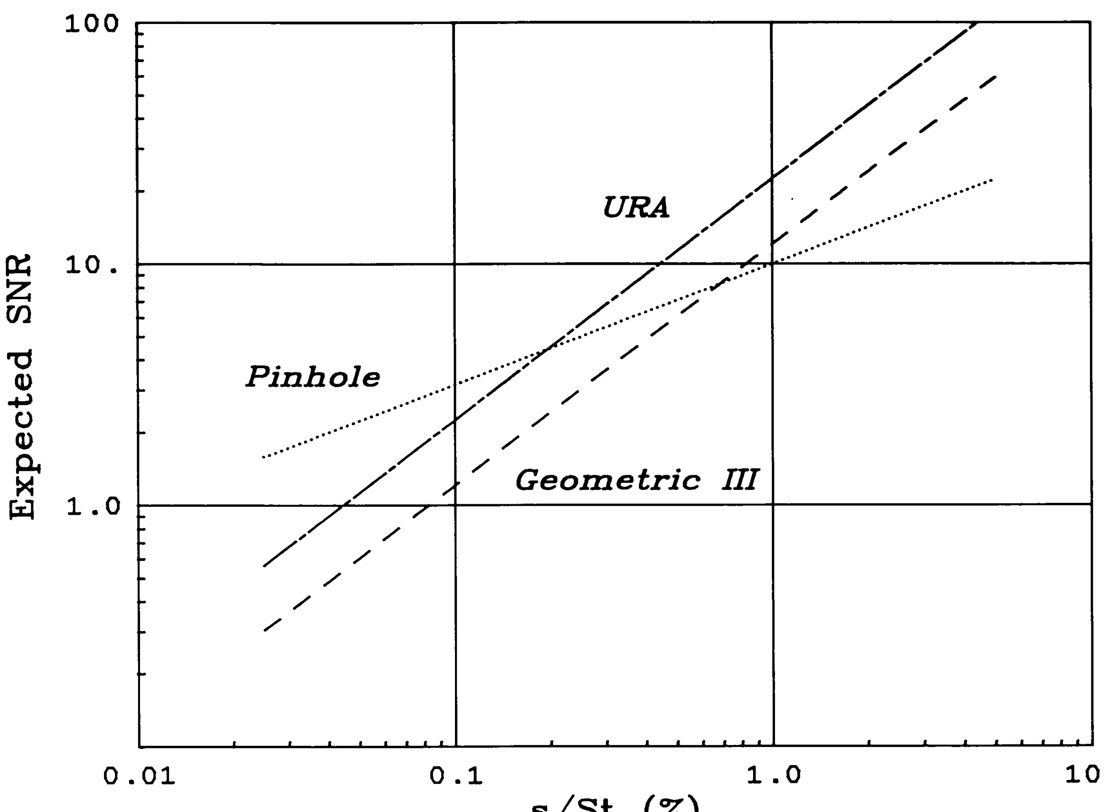

Fig. 3.9. A theoretical comparison between the expected performance (SNR) of a 50% transparent 31 × 33 URA, a 12% transparent 31 × 31 geometric pattern and a single pinhole mask (transparency of ≈ 0.1%) assuming no detector background (Gottesman and Schneid, 1986).

in the reconstructed image of a point source for systems, with the same detector area and intrinsic angular resolution, employing different mask designs. The evaluation assumed no unmodulated detector background, the object consisting of a point source superimposed on a uniform sky flux. For situations of very low contrast, in which the background counting rate dominates the source counts, it can be seen that the pinhole camera provides the best response, but this situation is rapidly reversed as the relative source intensity increases. As each of the complex mask designs is 'perfect', the difference in reconstructed SNR depends mainly on the transmission of the mask pattern, and hence the number of counts detected. For the URA and PNP, however, the structure of the modulated background has no effect on the predicted SNR, the variance of the background being given by the square root of the total detected counts, whereas for the geometric patterns the disuniformity in the weighting terms of the decoding array leads to a dependence on this parameter (Gourlay and Stephen, 1983; Gottesman and Schneid, 1986). Figure 3.10 shows the reconstructed images obtained from simulated observations of two point sources with four different mask designs. A

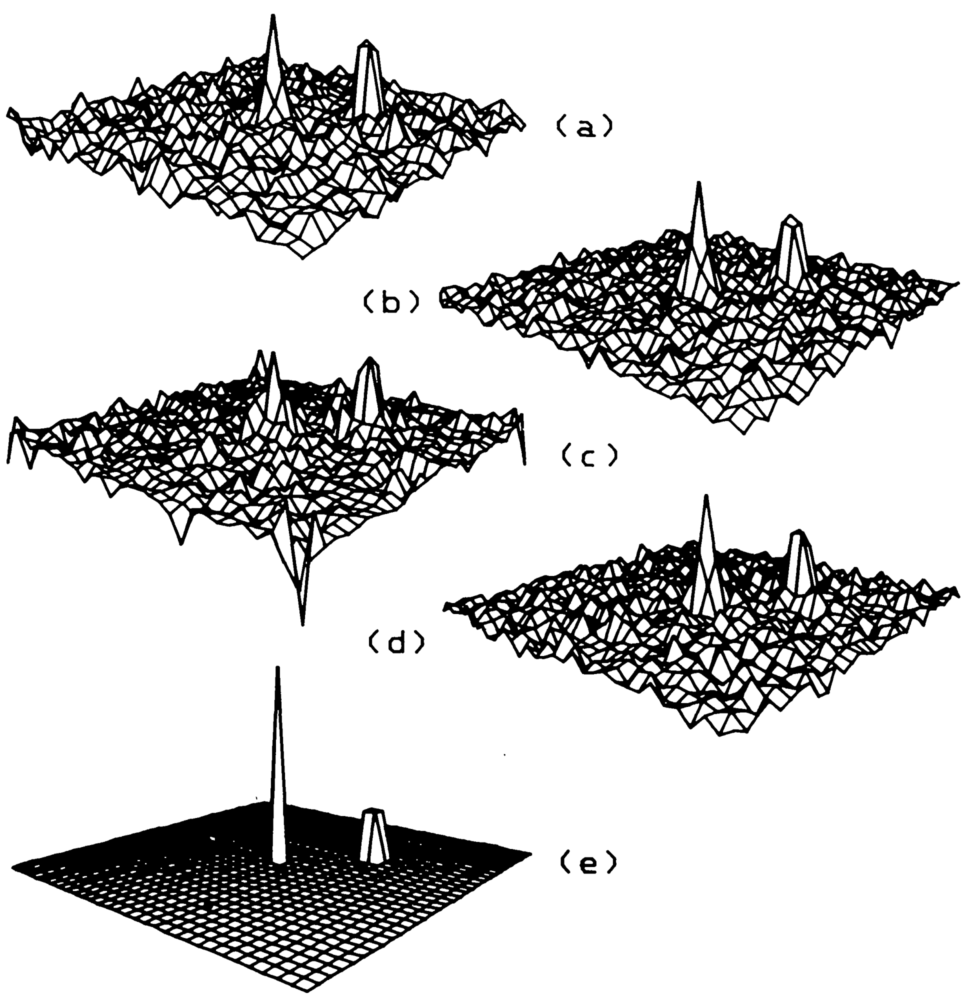

Fig. 3.10. Simulated images of the two source distribution (e) using: (a) a 31 × 31 random mask, (b) a 31 × 33 twin prime URA, (c) a 31 × 31 geometric design III pattern, and (d) a 31 × 31 PNP. The peak heights are all scaled to the same value so as to emphasise any background structure.

uniform detection plane background was assumed in each case, and mask designs of similar dimensions geometries were adopted for ease of comparison.

4. Some Design Constraints on Coded Aperture Systems

In the following sections some criteria that have important consequences on the design and ultimate efficiency of a coded aperture imaging device are outlined. They fall into three main categories: the detection plane, the mask itself and the conditions under which the device is to be used.

4.1. The Position Sensitive Detection Plane

For a given mask/PSD separation, the finite positional resolution of the PSD is the basic limiting factor for both the source location accuracy (SLA) and the angular resolution of the instrument. The accuracy to which it is possible to locate a point source in the field of view is determined by the ability to detect the edges of the shadow of the mask elements and thus, for a given statistical significance of the data, is purely dependent on the detector performance. In particular the relationship is of the form:

$$\Delta\omega \sim \frac{\sigma_d}{H \times \mathrm{SNR}}$$

where σ_d is the detector spatial resolution, H the mask/PSD separation, and SNR the statistical significance of the source image. Figure 4.1 indicates the expected SLA for

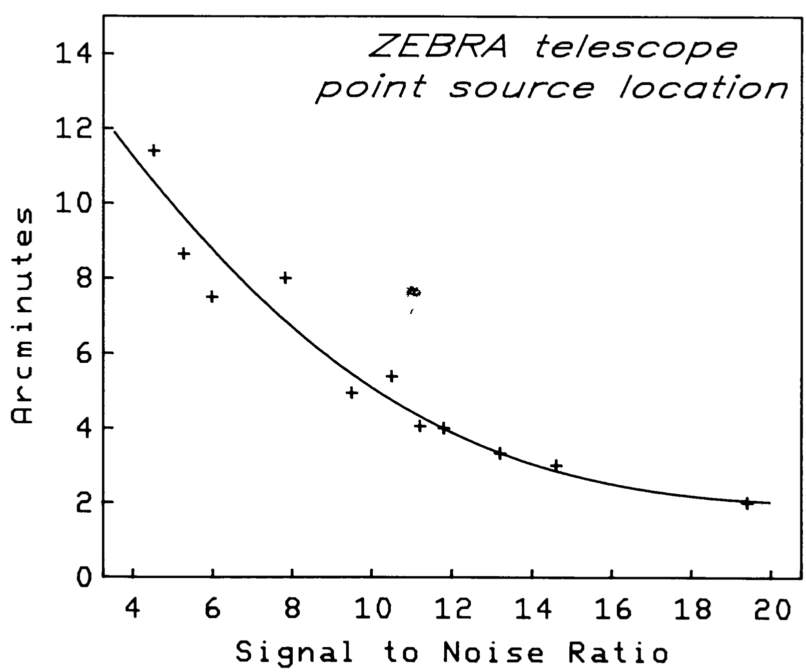

Fig. 4.1. The point source location accuracy of a coded aperture instrument depends on the reconstructed signal to noise ratio of each source. The picture shows data (+) obtained in laboratory tests with the ZEBRA position sensitive detector (Butler *et al.*, 1985).

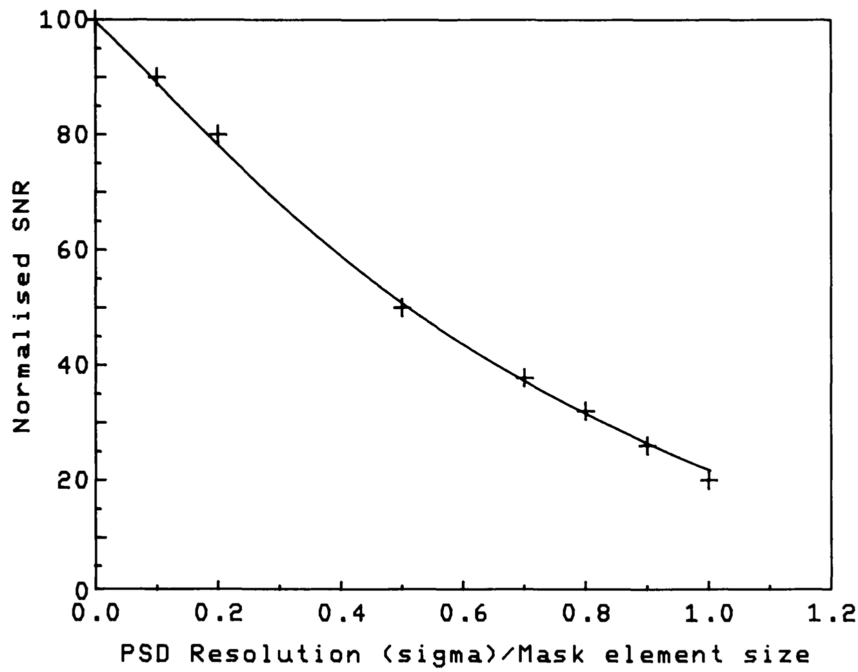

Fig. 4.2. The decrease in SNR from misallocation of photons to neighbouring pixels due to the finite spatial resolution of the PSD as a function of mask element dimensions. In order for the loss to be less than 50% the mask element size must be at least twice the spatial resolution (σ).

realistic values of these parameters. The angular resolution, on the other hand, is primarily dependent on the angle subtended by a mask element at the PSD and, hence, on the mask element dimensions, but the maximum resolution obtainable, or minimum element size usable, is dictated by the positional resolution of the PSD. This is because for a particular value of this resolution the smaller the mask elements are, the more effect that random errors in the positioning of detected events will have. Figure 4.2 shows the reduction in SNR which occurs for a single point source in one pixel as the mask element dimensions are changed. However, this circumstance will not affect the source flux evaluation. In fact, it can be shown (Charalambous *et al.*, 1984a) that the effect of a finite uniform spatial resolution over the detection plane is just a 'defocussing' of the image and, therefore, the intensity under the peak of the SPSF is retained, whilst the sensitivity of the instrument is reduced. The optimum compromise between angular resolution and sensitivity is obtained when the mask element sizes are such that no addition of adjacent pixels is necessary to obtain a reasonable SNR, i.e., the binning in the detection plane should be optimised depending on the strengths of the sources to be imaged (Miyamoto *et al.*, 1981). (This must not be confused with having detector pixel elements smaller than the mask element shadows, that is valuable for point source location.)

Another important aspect of PSD performance is the uniformity of efficiency and resolution across the plane. Variations in either of these parameters will have detrimental effects on the image quality and must be kept to a minimum, but it is rarely possible to eliminate them entirely. As described above, a uniform spatial resolution across the PSD results in a simple blurring of the image, but the effect of a differential resolution is to produce structures across the entire deconvolved picture, in particular 'ringing' around edges.

The most common type of efficiency variation occurs when the PSD is constructed from an array of detectors. Apart from the differences in the intrinsic efficiency of each detector, there is usually some part of the detection plane which is not sensitive – a 'dead' area – such as might be produced by the metal housing around scintillation crystals (see, for example, the ZEBRA balloon borne low-energy gamma-ray telescope: Boella *et al.*, 1986, and Section 5.5), or from the use of an array of cylindrical detectors (e.g., the proposed GRASP satellite in Section 5.6). A similar effect is induced by support structure in the detection plane. The latter is not a problem due to the inherently robust nature of coded aperture imaging to localised PSD anomalies (Charalambous *et al.*, 1984a; Hammersley and Skinner, 1984; Sims *et al.*, 1985), while two techniques have been applied successfully to overcome the former problem. These are: (1) applying a normalisation between the different detectors (McConnell *et al.*, 1987a) and (2) imaging the same field of view with two mask patterns one being the binary complement of the other (mask/anti-mask) (McConnell *et al.*, 1982). The first of these methods appears to be the more practical as it does not involve moving large masses during observations. Indeed the DGT telescope of New Hampshire (see Section 5.5) was originally planned as a mask/anti-mask system but the complexities involved led to the abandonment of this idea in favour of a simpler system and post-processing, one result of which is shown in Figure 4.3. By careful design, however, it is possible to minimize the amount of movement necessary to implement the latter method (see the GRIS telescope in Section 5.5).

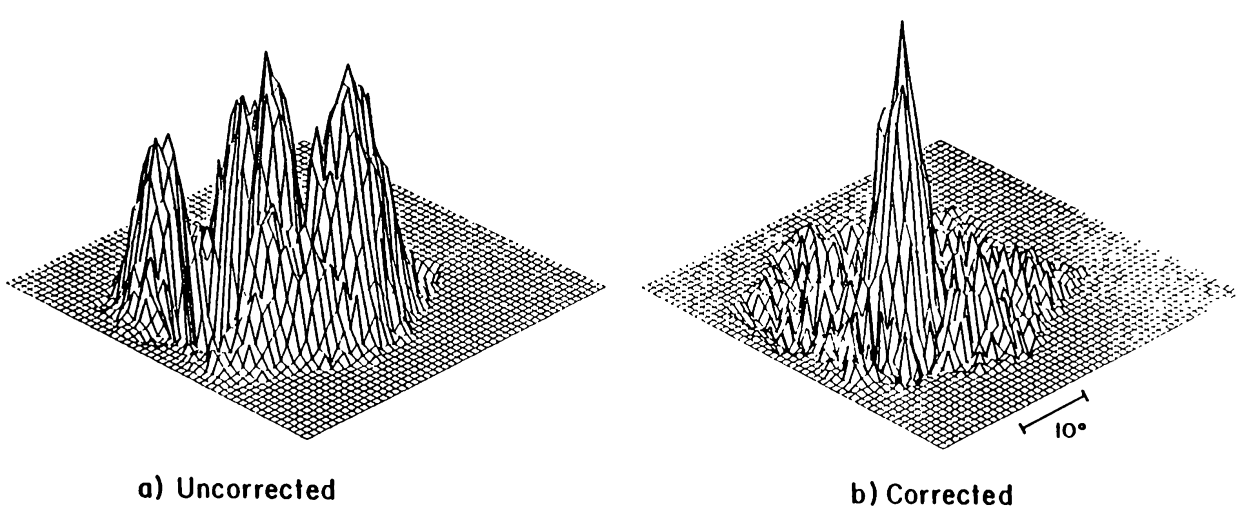

Fig. 4.3. (a) An image of the CRAB supernova remnant obtained by the DGT telescope showing the effect of different intrinsic counting rates in each element of the detection plane and (b) the same image after normalisation (McConnell *et al.* 1987).

4.2. The coded aperture mask

In a coded aperture system designed to produce images over a wide range of photon energies, the opaque mask elements vary in absorption efficiency with respect to photon energy, for instance passing through a minimum at about 2–3 MeV for high Z-materials. The increased transmission of unwanted photons at these energies will inevitably lead to a degradation in image quality. It is not always possible, however, to increase the mask element thickness until the desired opacity is achieved over the entire energy range of interest, due to the large weight and collimation effects associated to the use of a thick mask. For oblique angles of incidence some of the photons which would pass through an open element will be stopped by a neighbouring closed element, thus limiting the effective field of view of the instrument. To reduce this effect the profiles of each element may be rounded (Butler *et al.*, 1984), the only problem being that for sources close to the centre of the field of view this can lead to a loss of definition at the element boundaries – information which otherwise could be used for point source location purposes.

A similar problem occurs when a practical mask has to be constructed. The vast majority of optimum mask designs have isolated elements within the pattern, requiring a supporting structure (although see Giles, 1981, for some self-supporting URA designs). In general this implies that in the positions of the open elements some material is present.

For masks based on 2×2 mosaics of URA's, both the above cases may be dealt with in terms of the expected SNR in an image of a point source (Charalambous *et al.*, 1984a):

$$\mathrm{SNR}_{jk} = \frac{MS_{jk}(T_o + T_c) + S_{jk}T_c}{\{MS_{jk}(T_o + T_c) - S_{jk}T_c + (M(T_o + T_c) - T_c)S_t + NB\}^{1/2}}\,, \tag{4.1}$$

where the mask has N pixels, M of which are transparent ($N = 2M - 1$), the source strength is S_{jk} counts/mask element, the background is B counts/pixel, T_o and T_c are the transmissions of the open and closed elements, respectively, and S_t is the integrated intensity of all other sources in the field of view. It is interesting to consider two limiting conditions for Equation (4.1): for the case of perfect opacity of the closed elements, no background or background sources Equation (4.1) reduces to:

$$\mathrm{SNR}_{jk} = (NT_o S_{jk})^{1/2} \tag{4.2}$$

which is equivalent to imaging a source of reduced strength ($T_o S_{jk}$) with a perfect mask. Where the open elements transmit 100% of the incident radiation, under the same conditions we get:

$$\mathrm{SNR}_{jk} = \frac{(N - (N - 1)T_c)S_{jk}^{1/2}}{(N + (N - 1)T_c)^{1/2}}\,. \tag{4.3}$$

The term incorporating T_c in the numerator is responsible for a reduction in peak height, whilst the equivalent term in the denominator represents the increased variation in the background.

The presence of a massive aperture mask near the detection plane has also been considered a possible source of background contamination, and for this reason it has been suggested that the mask be constructed from active materials so as to provide anti-coincidence shielding (Johansson *et al.*, 1980). Both Butler *et al.* (1984) and Owens *et al.* (1985) have shown, however, that although the absolute count rate over the PSD may be slightly increased by neutron activation of the mask elements, for mask/detector separations of practical interest this contribution may be considered to be spatially uniform over the PSD (Figure 4.4) and the extra complication involved in employing an active mask is probably not justified.

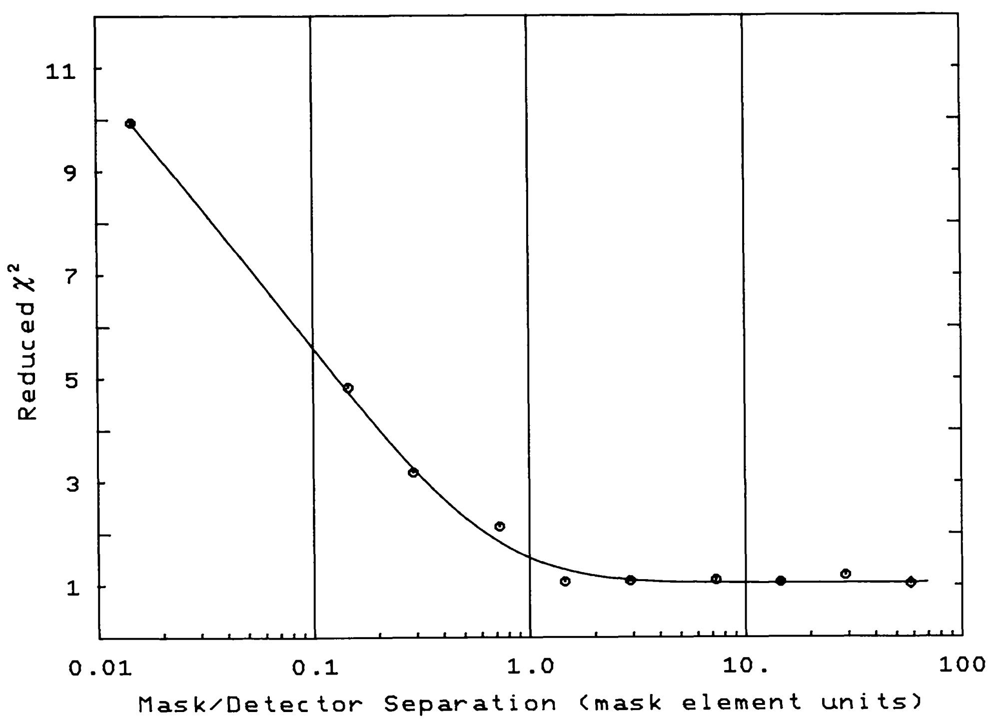

Fig. 4.4. The modulation of the background counting rate across the detection plane introduced by the interaction between an isotropic photon flux and the coded aperture, measured by the reduced χ^2 of the resulting distribution in comparison with a flat background with the same mean counts per pixel. The background modulation is given as a function of the mask/detector separation expressed in number of mask elements. The (●) data are obtained from MonteCarlo simulations of the ZEBRA telescope configuration (Butler *et al.*, 1984).

Also related to the aperture configuration is the degree of alignment between the mask and the PSD. In comparison to other methods of obtaining images, the coded aperture technique is very insensitive to this type of misalignment, unless it is in the form of a rotational deplacement. Quantitatively, a horizontal translational misalignment (or motion) of an amount r will produce a mis-positioning (or blurring) of a source in the field of view given by:

$$\Delta\psi = \operatorname{arctg}(r/H)\,,$$

where the mask/detector distance is H.

Similarly a vertical displacement of ΔH will give rise to an uncertainty

$$\Delta\phi = \operatorname{arctg}\left(\frac{\Delta H \operatorname{tg}\phi}{H \sec^2\phi + \Delta H}\right),$$

for a source at angle ϕ to the centre of the field of view.

These effects are small as may be seen if we consider a system with $H = 3$ m; $\phi = 5°$, $r = 1$ cm, and $\Delta H = 5$ cm; then from the translation $\Delta\psi = 10$ arc min and from the vertical displacement $\Delta\phi = 5$ arc min.

The effect of a rotational misaligment is more severe in that the entire image is affected and systematic errors occur in the background leading to the presence of 'ghost' sources. The degree of misalignment acceptable is strongly dependent on the instrument dimensions (Charalambous *et al.*, 1984a, b; Hammersley, 1986).

4.3. Instrument Surroundings

The presence of a non-uniform background distribution across the PSD can lead to large systematic fluctuations in the deconvolved image (Figure 4.5). The nature and intensity of these fluctuations are dependent not only on the background counting rate and distribution but also on the mask pattern and deconvolution method employed. For severe nonlinearity of the background counting rate, equivalent to strong variations in detection efficiency across the PSD, pre-processing of the data before deconvolution

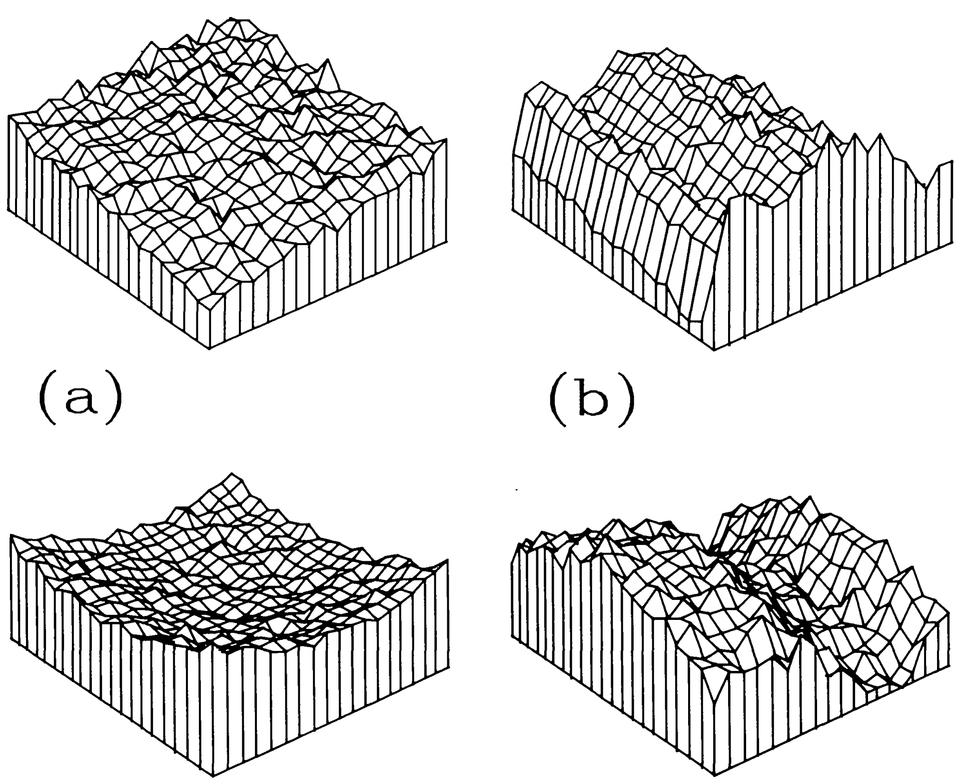

Fig. 4.5. Two examples of the manner in which non-uniform background distributions (a) affect the decoded image (b). In both cases the non-uniformity is 10% of the mean value.

is necessary. This can either take the form of filtering in the frequency domain or the PSD may be considered as a set of discrete detectors and the normalisation/anti-mask techniques described in section 4.1 may be applied.

4.4. Vignetting of Sources

The likely number and distribution of the sources within the field of view must also be considered when designing a practical system. At low energies (up to a few tens of keV) a grid collimator may be employed to limit the field of view of each element of the detection plane (Sims *et al.*, 1980), and at very high energies (at a few tens of MeV) the directional information obtained from the PSD allows some extra background rejection (Thompson, 1986), but in the low-energy gamma-ray regime neither of these techniques are practicable and, therefore, sources outside of the intended field of view may be seen (Vignetting). Systems employing jointly time- and spatial-multiplexing, e.g., rotating HURA's, are virtually immune from this problem (Cook *et al.*, 1984), whilst instruments employing static masks can suffer from it. Totally uncoded sources merely increase the background level over the PSD. Problems instead arise when a source casts an incomplete shadow of the aperture onto the detection plane. The reconstructed image of vignetted sources consists of a peak with false intensity superimposed on a very high structured background that produces strong interference between the different flux contributions (Figure 4.6). Moreover, mosaiced masks suffer from the additional problem that the recorded shadowgram, when decoded by direct methods, is consistent

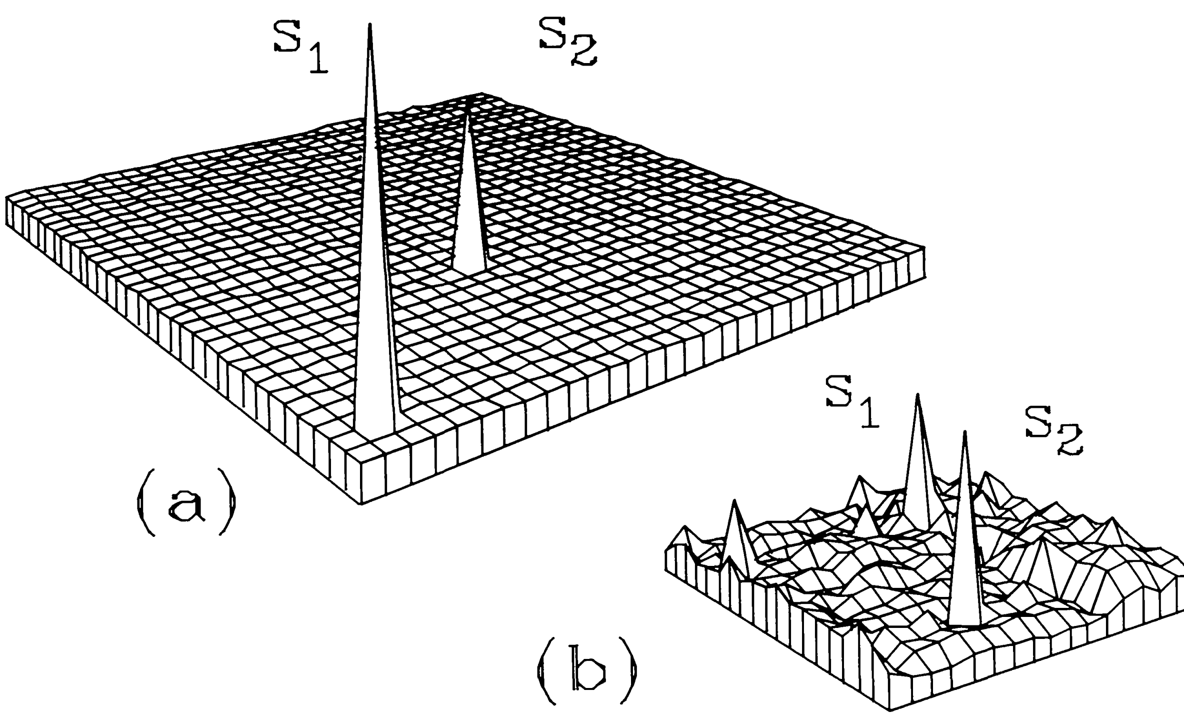

Fig. 4.6. Effect of source vignetting: (a) true position and intensity of two sources, one (S_2) in the FCFV and the other (S_1) in the PCFV. (b) reconstructed image of the FCFV using correlation (assuming no detector background).

with up to 9 point source locations, only one of which is in the FCFV (Maggioli *et al.*, 1984; Badiali *et al.*, 1982). This problem may be tackled by means of: (a) using advanced deconvolution methods (e.g., Wiener filtering, Maximum Entropy Method) (Willingale *et al.*, 1984; Sims *et al.*, 1984); (b) performing a statistical analysis of the shadowgram (Ducros and Ducros, 1984); (c) decoding each image by a correlation with suitably altered arrays in order to identify possibly vignetted sources (Maggioli *et al.*, 1984; Stephen *et al.*, 1987); or (d) making use of the different behaviour between fully- and partially-coded sources occurring with a rotating telescope (Badiali *et al.*, 1985). This last technique requires a rotating, or oscillating, telescope – a situation that is not always desirable from the point of view of sensitivity.

5. Coded Aperture Instrumentation in High-Energy Astronomy

5.1. Introduction

Many of the different types of coded apertures, as described in Section 3, have been, or are being, employed for obtaining images of celestial sources of high-energy emission. In the following sections we present a review of coded aperture telescopes, of the past, present, and forthcoming generation, along with the results which have already been produced with this technique. The instruments are presented and discussed according to the type of mask employed. Their main characteristics are listed in Table I.

TABLE I

Expt.	Vehicle	Mask	PSD	A(cm^2)	Energy	Ang. Res.	FOV	Notes
	Skylark	Fresnel	MWPC		< 50 keV	16"		Failed
ASM	Ariel V	Pinhole	"	1	2.5-7.5 keV	2°	4 × 180°	Flown
"	Spc. Stat.		"	6 × 1	"	"	All sky	Proposed
	Satellite	Random	"	14000		6°	2.7π str	"
	"	"			25-100 keV	23'	"	"
	Skylark	"	Film		.6-1.6 keV	23"		Flown
Gam Cam	Balloon	"	NaI	1200	30-600 keV	2°	120°	Failed
HXT	TENMA	URA		2x54		1°	40°	Flown
Gamma-1	Satellite	"	Spark	2500	> 50 MeV	0.2°	5.7°	1988
SL 1501	Skylark	"	MWPC	513	2.2-10 keV	2.5'x 21'	4°	Flown
XRT	Shuttle	"	MWPC	2048	2.5-25 keV	3'x12'	6.4°	"
WFC	SAX	"	"	2x500	2-30 keV	5'	20°	1990
"	Salyut	"	"	625	"	2'	7.5°	1987
TXC	Balloon	"	"	470	20-150 keV	5 × 4°	37 × 38°	Flown
EXITE	"	"	NaI	4x900	20-300 keV	22'	3.4°	1988-
SIGMA	GRANAT	"	"	1024	0.2-2 MeV	13'	8°	1988
DGT	Balloon	"	BGO	715	0.1-10 MeV	3.8°	15 × 23°	Flown
ZEBRA	"	"	NaI	2x2550	0.2-10 MeV	1°	7 × 9°	1988
GRETEL	EURECA	"	"		0.1-10 MeV	< 1°	5°	Proposed
GRIS	Balloon	"	Ge	232	.02-10 MeV	4°	9 × 15°	1986/7
CAMTRAC	Satellite	"	Drift	5000	> 50 MeV	10'	30°	Proposed
GRIP	"	HURA	NaI	1300	.03-5 MeV	0.6°	20°	Flown
GRASP	Satellite	"	CsI/Ge	3300/900	.02-100 MeV	< 1°	"	Proposed

5.2. Non-pinhole masks

Although Fresnel Zone Plates have been applied usefully in the fields of optical astronomy and spectroscopy, in high-energy astronomy only one attempt has been made to construct an experiment based on this type of coded aperture (Boyd, 1973), operating up to about 50 keV with an angular resolution of 16 arc sec. The instrument was initially proposed for use on HEAO–C, but eventually an attempt was made to launch it on board a Skylark rocket which unfortunately failed.

5.3. Pinhole cameras

The All-Sky Monitor (ASM) on board Ariel V, although not strictly a coded aperture system, was the first satellite-borne X-ray astronomy experiment capable of producing true images, while at the same time being one of the smallest (effective aperture 1 cm^2) and lightest (≈ 2 kg) experiments ever flown (Holt, 1976). The experimental arrangement consisted of two position sensitive proportional counters set 90° apart, each with an associated pinhole. The response function of each aperture was in the form of a fan beam of $4° \times 90°$, producing a combined response of $4° \times 180°$, which, in conjunction with the 10 r.p.m. spacecraft rotation allowed the entire sky to be mapped once per rotation. Although the detector positional resolution (1 mm) and aperture/detector distance (20 cm) combined would suggest a maximum angular resolution of the instrument of about 20 arc min, the size of the pinhole necessary in order to obtain a reasonable SNR dictated a resolution of $\approx 2° \times 2°$ and the on board memory store reduced this further ($10° \times 10°$), if used for all-sky coverage. Among the results from the ASM were the discovery of several X-ray transient sources, and of a long-term 5.6-day variation in Cyg X-1 (Holt *et al.*, 1976).

Recently, with the interest being shown in the U.S.A. and elsewhere for a permanently manned space station, a proposal has emerged for the construction of a semi-permanent X-ray ASM to be sited on such a facility (Holt and Priedhorsky, 1986). The design suggested consists of an array of six independent cubic pinhole cameras, of side approximately 30 cm, providing all sky coverage, with a point source location accuracy of a few arcminutes and a sensitivity of a few millicrabs for a 10^5 s observation.

5.4. Random masks

Although Dicke (1968) and Ables (1968) made the first reference to the application of random mask cameras to high energy astronomy, these were really only suggestions on using the technique rather than instrument proposals, that were amplified upon in the work of Palmieri (1974). One of the first suggestions for an X-ray satellite employing coded apertures was by De Jager (1974) who described a polyhedral (> 6 sides) design with coded aperture telescopes mounted on each face. Each individual telescope would have employed a position sensitive proportional counter (at that time large area devices were relatively new) in conjunction with a two-dimensional random mask. Another early proposal for the use of coded apertures for an X-ray satellite was in 1975 when Helmken *et al.* (1975) suggested employing three one-dimensional random slot cameras as a wide field of view instrument for detection and location of γ-ray bursts. The geometry was slightly peculiar in that the masks were arranged on a curved surface around a Xenon PSD, producing a wide field of view (2.7π steradians).

In 1972 a random pinhole array was successfully used for solar X-ray photography on board a Skylark rocket in a multi-aperture camera operating in the soft X-ray range (0.64–1.6 keV) (Blake *et al.*, 1974). The camera incorporated two random aperture plates with complementary distributions of holes (i.e., a mask anti-mask combination). Each mask was a 61×61 lattice array of 50 μm cells half of which were punched with 25 μm holes for a open fraction of $\frac{1}{8}$th of the total area. A film detector was placed 23 cm from the aperture leading to an angular resolution of the system of 23 arc sec. The hole distribution of the random array was optimized to guarantee that the SPSF had minimum-amplitude sidelobes. The results consisted of maps of solar X-ray active regions.

More recently an attempt was made to fly a balloon borne imaging gamma camera for γ-ray burst detection in the range 30–600 keV. The telescope consisted of a circular NaI crystal (≈ 1200 cm^2), viewed by an array of 19 photomultipliers, in conjunction with a 50% transparent random mask of more than 10000 elements with an area 20 times larger than the detector (Ventura *et al.*, 1984). To increase the chance of burst detection during the limited observation time allowed by a balloon flight, the instrument was designed to have a large FOV: the FCFV was a cone of about 120° opening angle with an angular resolution of $2° \times 2°$. In designing the random pattern of the mask particular care was devoted to minimizing the variation of aperture seen by the detector at any direction within the FCFV in order to maintain as uniform as possible the system sensitivity. In the implemented pattern the open fraction of each working zone ranged from about 57% for the zenith to 42% at 60° (Horstman *et al.*, 1984). The instrument flew from the Milo base (Sicily) in 1983, but did not produce data because of a mechanical failure of the detector window.

5.5. Uniformly Redundant Arrays (URA)

5.5.1. *One-Dimensional Masks*

The Japanese scientific satellite Astro-B (Tenma) (Tanaka *et al.*, 1984) was launched on 20 February, 1983, and followed on from the success of their first X-ray satellite Hakucho (Astro-A). Although the main experiment on board was a set of ten gas scintillation proportional counters there was also a transient source monitor which itself comprised two experiments: a collimated (fan-beam) scanning detector and two one dimensional Hadanard X-ray Telescopes (HXT's) set orthogonally so as to simulate a two-dimensional device. The apertures of each telescope consisted of a length 15 Hadamard mask. Although the satellite functioned well (Tanaka, 1984) results from the HXT have not been published yet.

At higher energies, the Soviet–French Gamma-1 satellite in its original form was a bare high-energy gamma-ray (> 50 MeV) spark chamber instrument (Bazer-Bachi *et al.*, 1977), but in later configurations a removable coded aperture mask was introduced so as to increase the resolving power at the lower end of its spectral range (Akimov *et al.*, 1985). The mask consists of two one dimensional patterns, again set orthogonally as in Astro-B, but with both patterns being viewed by different parts of the same detector. The mask itself is constructed from tungsten, 10 mm (about 2.7 radiation lengths) thick, and it is surrounded by plastic anticoincidence scintillator. The basic pattern is derived from a 50% transparent cyclic difference set of length 144, with four periods in one direction and two in the other (Prilutsky, 1979). The inherent angular resolution of the spark chambers precludes any ambiguity caused by the multiple periods. With a basic element size of 1 mm and a mask/centre of detector distance of 300 cm, the angular resolution will be about 0.2°, an order of magnitude better than the resolution obtainable at 50 MeV with the spark chamber alone. Gamma-1 is scheduled for launch in 1988 from the U.S.S.R.

5.5.2. *Two-Dimensional Masks*

One of the earliest imaging instruments for high-energy astronomy using an URA was the Birmingham instrument known as SL1501 which was flown on a Skylark rocket in June 1976 (Proctor *et al.*, 1979). During the mission the galactic centre region was observed and even though the observation time was very short (≈ 350 s) it was able to distinguish several different sources of emission in the energy range 2.2–10.2 keV (Proctor *et al.*, 1978). The geometric arrangement of the instrument consisted of a 2×2 cycle URA mask with a detector of about the same area implemented in such a way that the central quarter of the detector viewed a fully coded shadowgram. During the data analysis the signal from the vignetted detector region was also utilized to produce an independent reconstructed map. The URA mask was based on an m-sequence of length 1023 folded into a 11×93 basic pattern array. As the mask was 186 cm away from the detector and the mask element size was 0.14×1.14 cm, the geometric resolution (FWHM) was about 2.5×21 arc min and the FCFV $\approx 4° \times 4°$. The PSD was a multiwire proportional counter (geometric area 513 cm^2) with positional resolution ranging from 0.12 cm at 2 keV down to 0.07 cm at 6 keV. A collimator array with the same period of the mask was incorporated in the detector mechanical support.

The University of Birmingham (U.K.) also designed and constructed a coded mask X-ray telescope (XRT) which flew successfully on the Spacelab-2 Shuttle mission in July 1985 (Willmore *et al.*, 1981, 1986). The XRT consisted of a pair of telescopes (Figure 5.1), both based on Hadamard mask patterns – one a 31×33 array and the other with four times the resolution based on a 127×129 array, in conjunction with two proportional counters (Eyles *et al.*, 1987) having a total geometric area of 2048 cm^2. The telescope was operational in the energy range 2.5–25 keV with an angular resolution of $\approx 3 \times 12$ arc min. To date only preliminary scientific results have emerged from the mission (Harper *et al.*, 1987; Skinner *et al.*, 1987), with the main analysis still to be performed, however, quick look data already show some interesting results (see Figure 5.2a, b).

The X-ray astronomy satellite SAX (Scarsi, 1984) is at present in the phase B study development. One of the four types of instrument aboard is a wide field camera (WFC)

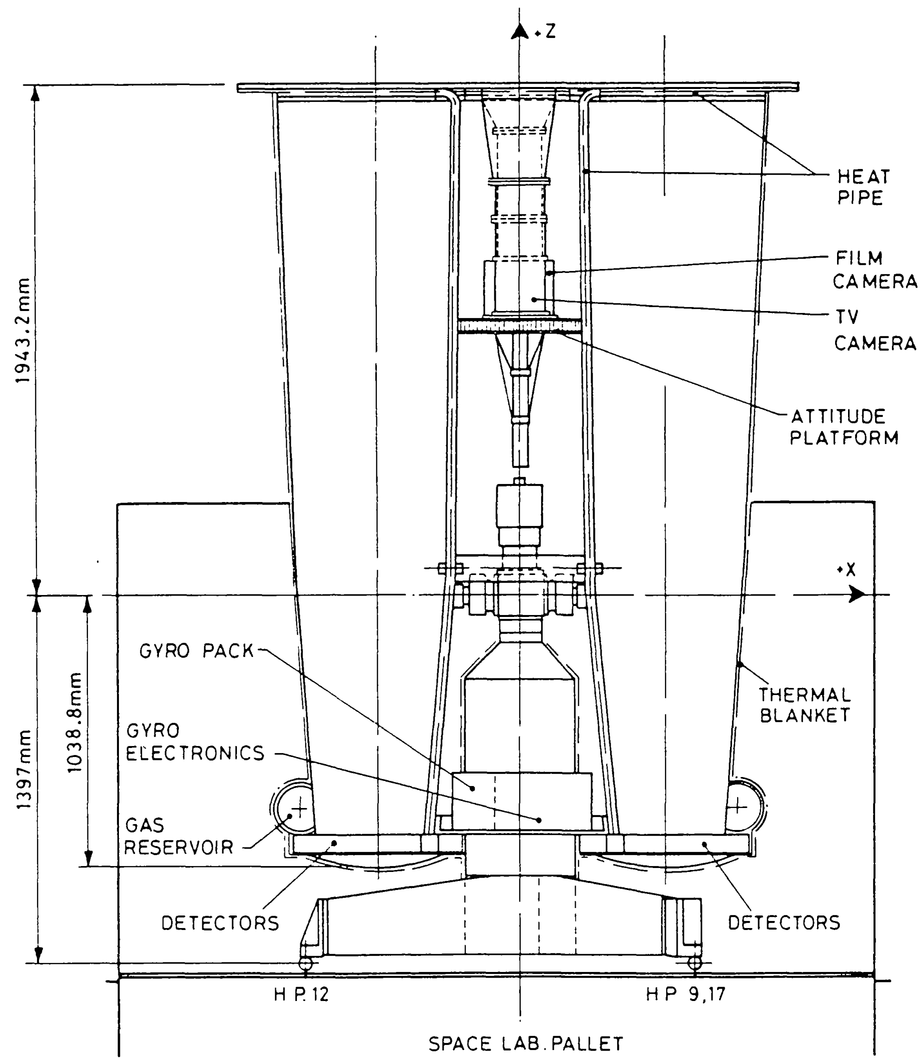

Fig. 5.1. General configuration of the XRT (Willmore *et al.*, 1984).

(Spada, 1983; Di Cocco, 1986) designed to provide on a continuous basis X-ray images of a large field of view (20° × 20° FWHM). Two of these WFC's will be on board SAX. The WFC apertures will be simple (i.e., not replicated) quadratic residues URA patterns of 255 × 257 square elements constructed from 25 cm × 25 cm thin plates of stainless steel coated with gold for improved absorption. They will be placed ≈ 70 cm from the detectors providing a geometric resolution of 5 arc min. The PSD's will be Xe/CO filled MWPC's with the same area of the mask and operating in the range 2–30 keV in the centre of the FOV and 2–10 keV over the full aperture. The average spatial resolution of the detector is about 0.05 cm compatible, for strong sources, with an error box of few square arc min.

A similar WFC is also one of the X-ray instruments on board the Soviet MIR mission launched in 1987. The WFC has an angular resolution of ≈ 2 × 2 arc min and a field of view (FWHM) of 7.5° × 7.5° (Brinkman *et al.*, 1983).

In August 1981 the Transient X-ray Camera (TXC), an imaging experiment incorporating an URA mask, was flown from Sicily (Ranieri *et al.*, 1981; Cardini *et al.*,

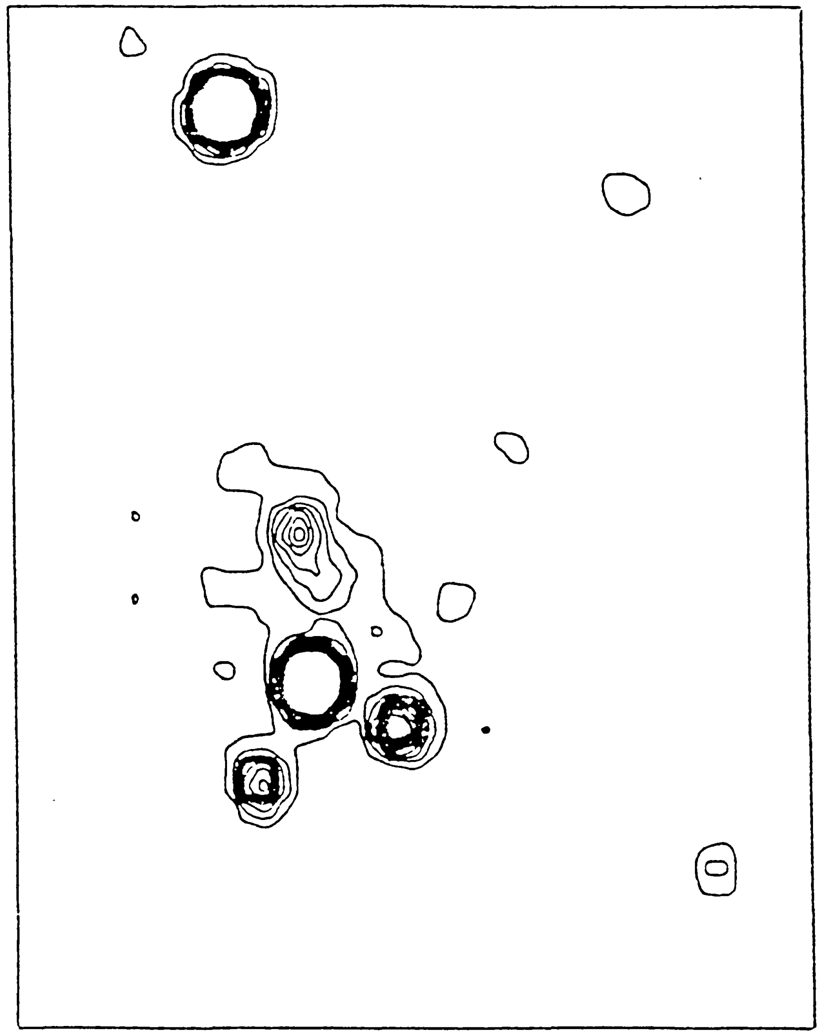
(a)

Fig. 5.2. Contour maps from the XRT in the 2.5–25 keV energy range (Skinner *et al.*, 1987): (a) the galactic centre region; (b) the Perseus cluster of galaxies.

1983). The telescope was designed for the hard X-ray region (20–150 keV), the detector being a Xenon MWPC (geometric area $\approx 470\ \mathrm{cm}^2$), with a spatial resolution of about 0.12 cm. The mask was a 2×2 cycle replication of a 7×9 Hadamard array and was situated 24 cm from the detector window supported by a plastic scintillator. Each element of the mask was a rectangle of 0.22×0.28 cm providing an intrinsic resolution of 5×4 square degrees and a FCFV of 37×38 square degrees. The mask-detector system was passively shielded with lead and copper. During the flight the TXC observed hard X-ray emission for about 3 min (Emanuele *et al.*, 1984). The subsequent analysis of the data allowed the reconstruction of the correct location of this emission and its association with a solar flare which occurred in the partially coded field of view of the telescope. The result was obtained by making use of the fact that during the flight the azimuthal angle of the telescope was smoothly oscillating ($\approx 200°$ in 4 min). In the data analysis phase an integration over a long exposure time was performed without despinning the data, thus all the background disuniformity was spread almost uniformly

(b)

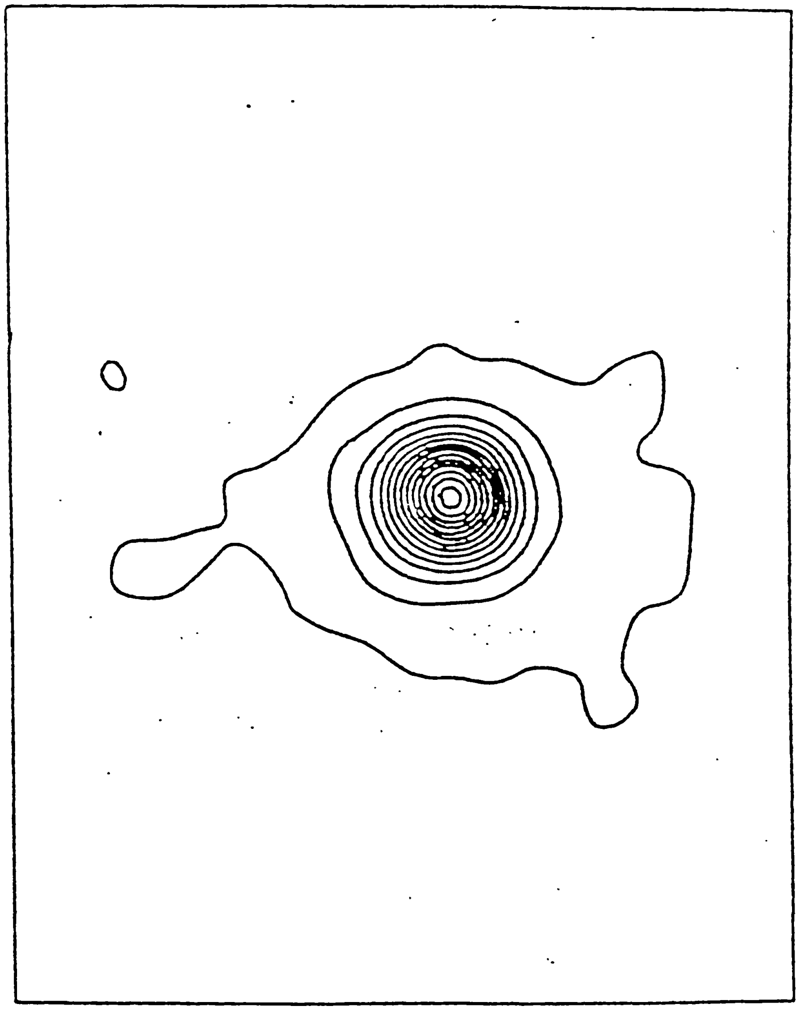

Fig. 5.2b.

over the PSD while the disuniformity due to vignetted sources were distributed along circular rings. (Badiali *et al.*, 1985; see also Section 4).

For imaging in hard X-ray astronomy another coded aperture instrument is currently under development: the Energetic X-ray Imaging and Timing Experiment (EXITE). Initially this instrument was proposed as a second experiment for the XTE satellite and/or for an entire Explorer mission (Grindlay and Murray, 1981) but the current version is forseen as a balloon borne experiment (Figure 5.3). The design consists of four identical units each with geometric area ≈ 900 cm^2. Each unit is an individual coded mask telescope (Garcia *et al.*, 1986) comprising: (1) a mask consisting of about 4×4 cycles of a basic 11×13 URA array, (2) a 3.4×3.4 square degree (FWHM) square collimator, and (3) a NaI crystal of 34 cm diameter and 0.64 cm thickness coupled with a two-stage imaging intensifier. The detector will operate in the 20–300 keV range with a spatial resolution ranging from 1.3 to 0.3 cm (FWHM), respectively. The mask element size has been chosen to be 1.3×1.3 cm, and the entire aperture will be made self-supporting by choosing as open elements squares with sides less than 1.3 cm for an actual open fraction of about 40%. The mask detector distance is foreseen to be

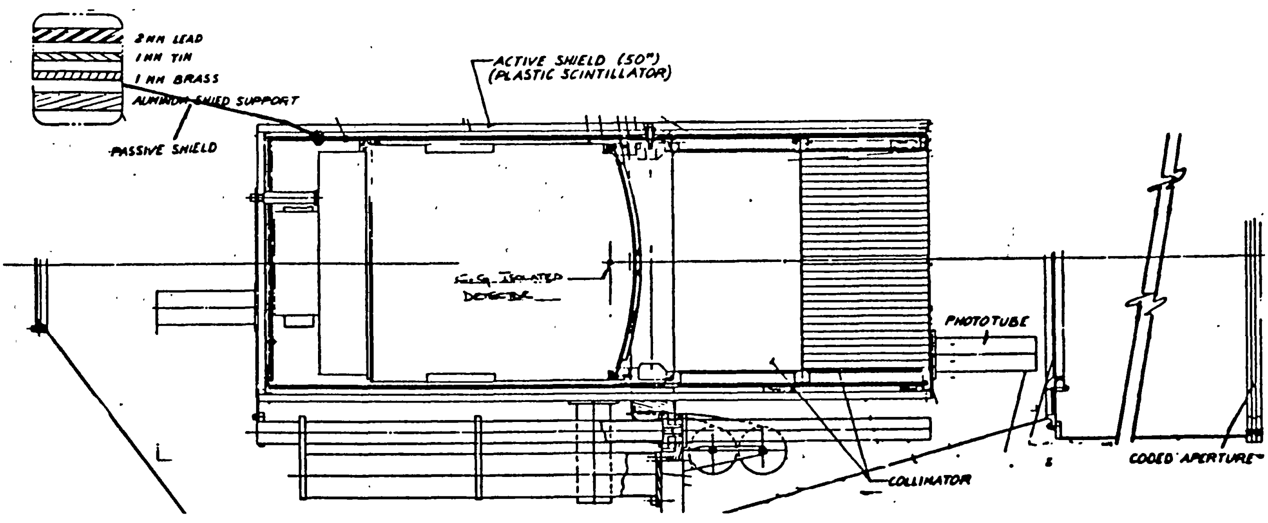

Fig. 5.3. Diagram of the EXITE telescope (Garcia *et al.*, 1986).

200 cm giving an intrinsic angular resolution of 22 arc min. The detector size ensures that at least 2 complete cycles of the mask will contribute to the detected shadowgram. Every cycle will be used to reconstruct an independent sky image, allowing the effect of non-uniformity of the background to be taken into account at the data analysis stage. Ambiguities will not arise from the multiple cycle URA because the Pb/Cu square collimator with the same spatial period of the coded aperture restricts the field of view (FCFV) at any point on the detector to just one cycle of the mask. EXITE will have a source location capability better than 2 arc min (Grindlay *et al.*, 1986).

The Franco–Soviet hard X-ray satellite SIGMA (Satellite d'Imagerie Monte-sur-Ariane) is designed to operate in the hard X-ray to low-energy gamma-ray range (20 keV–2 MeV). The PSD is a 1.25 cm thick NaI (Tl) Anger camera, actively shielded, with the mask situated at 2.5 m distance (Figure 5.4a). Initial designs envisaged the use of a 41×43 quadratic residues URA (in a 2×2 cycle form) thus implying an intrinsic angular resolution of about 10 arc min (Debouzy, 1983), but more recently (Mandrou, 1984) a 29×31 Fenimore URA design has been preferred with 13 arc min resolution (Figure 5.4b). This latter version has an element size of $9.6 \times 9.6 \times 15$ mm thick and 3×3 PSD pixels per mask element shadow. The mask is held in place by two 6 mm thick planes of carbon fibre. The PSD positional resolution of 4 mm (FWHM) will lead to very little data loss (see Section 4.1). The launch date is set for 1988 on board the Soviet GRANAT satellite.

At even higher energies (0.1–10 MeV) gamma-ray images have already been obtained from the Directional Gamma Ray Telescope (DGT) of the New Hampshire University (McConnel *et al.*, 1982). The acively shielded DGT detector consists of 35 Bismuth Germanate crystals (BGO) (5.1 cm diameter, 2 cm thick) arranged in a 5×7 array. The coded mask is positioned 84 cm above the detection plane and is a conventional 2×2 mosaic of a 5×7 quadratic residue URA. Each opaque element of the mask is a 5.6 cm $\times$ 5.6 cm block of 1.9 cm thick lead providing an angular resolution of

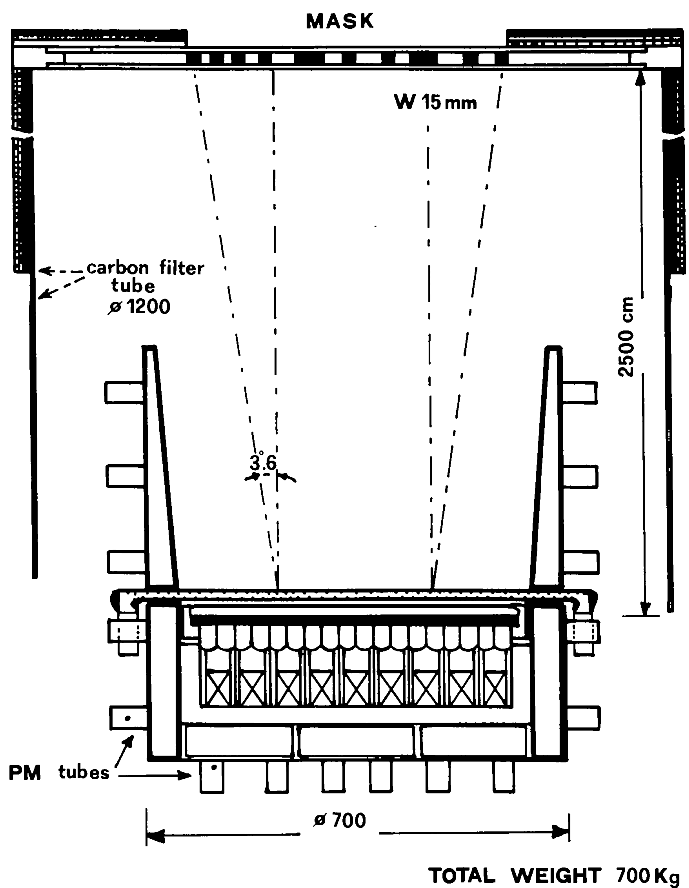

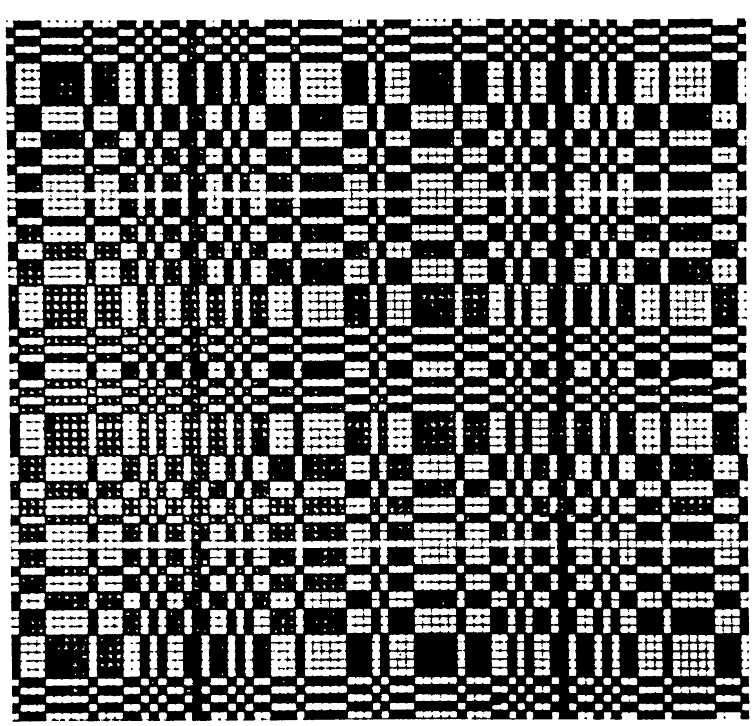

Fig. 5.4. The SIGMA telescope: (a) schematic view; (b) mask pattern (Debouzy, 1983).

3.8 × 3.8 square degrees and a FCFV of ≈15° × 23°. The original design of the telescope foresaw the use of an antimask to eliminate imaging problems arising from background disuniformities within the BGO array. The mask and antimask were to be mounted on opposite sides of the main gondola support arch and the detector could be rotated to view either one mask or the other (McConnell *et al.*, 1983). Mechanical difficulties in the implementation of the mask/anti-mask system led to the abandonment of this idea in the version of the DGT telescope flown successfully on 2 October, 1984 from Palestine, Texas. During this flight the galactic anticentre was observed and the first imaging data of the Crab and Cygnus regions will be published soon (McConnel *et al.*, 1987b, c; Owens *et al.*, 1987). In the analysis of the data, a major factor that seriously affected the reconstructed sky maps was the effect of systematic differences in counting rates (of the order of 5–10%) between the 35 BGO crystals. McConnel *et al.* (1987d) describe the algorithm used to renormalize the background across the detector units by means of which a successful location of the Crab to an accuracy of 12 arc min (1σ) over the 200–600 keV range was achieved (Figure 4.3).

The coded mask telescope ZEBRA, developed by a collaboration between 3 Italian groups (Istituto Te.S.R.E., Bologna, IFCTR, Milano, IAS, Frascati) and Southampton University in the U.K., will operate in almost the same spectral range (0.2–10 MeV). This balloon-borne instrument will be flown from New Mexico in the spring of 1988 (Villa *et al.*, 1987). In Figure 5.5 a schematic view of the ZEBRA arrangement for the first flight is presented, showing only one mask-detector unit, while the final design calls

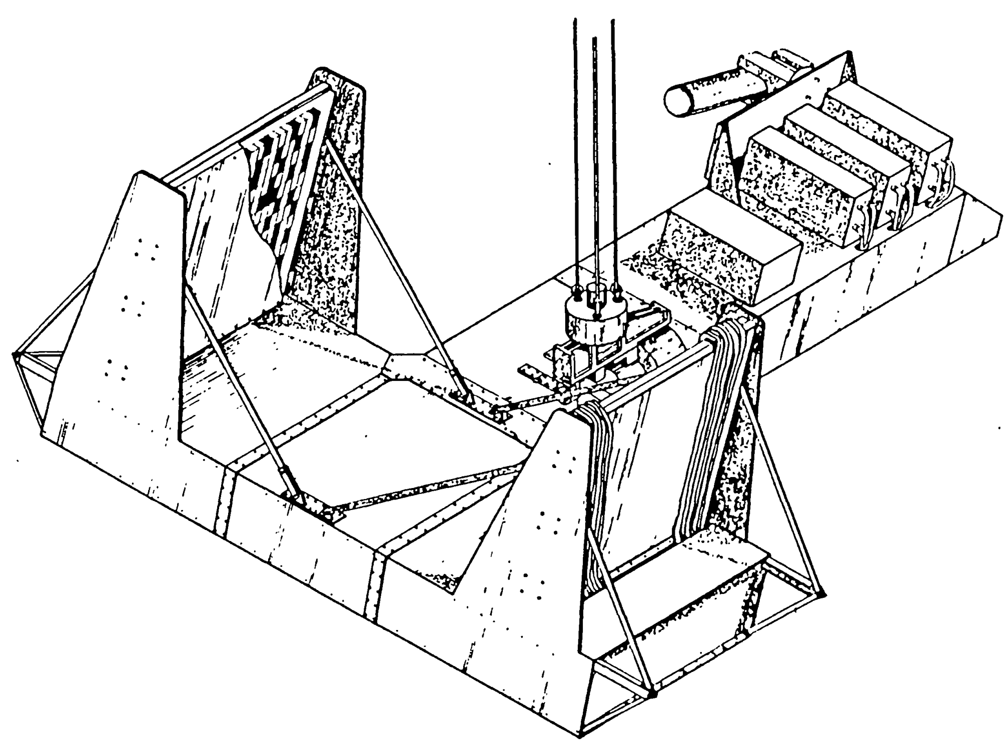

Fig. 5.5. Schematic view of the ZEBRA telescope in the first flight configuration (i.e., employing only one of the two mask/detector modules of the nominal configuration).

for two identical modules mounted on either side of the platform support. The ZEBRA PSD consists of 9 NaI bars of 55 × 5.8 × 5 cm thick read at each end by a PM tube. The surface of the PSD bars have been treated so to attenuate exponentially the scintillation light along the length allowing the reconstruction of the photon interaction positions and the energy loss by combining of the two PM signals (Charalambous *et al.*, 1984b). The PSD is then surrounded by 13 nonposition sensitive NaI bars and plastic scintillator for anti-coincidence purposes. The position resolution along the bars ranges from 1.9 to 3.4 cm (FWHM at 661.6 keV). The mask is an usual 2 × 2 replication of a 9 × 7 Hadamard basic pattern constructed from 2 cm thick Tungsten blocks of 6.7 × 7 cm size, and is placed at 350 cm from the PSD. The FCFV of each module is 7° × 9° with an angular resolution of 1 square degree. Both mask and detector are rigidly mounted upon 5 cm thick carbon fibre planes. The size of each mask element along the bar corresponds to exactly 16 channels in the output of the flight electronics leading a maximum point source location accuracy of a few arc min (Butler *et al.*, 1985) and a sky map of 9 × 112 pixels. In Figures 5.6 and 5.7 the images of two typical

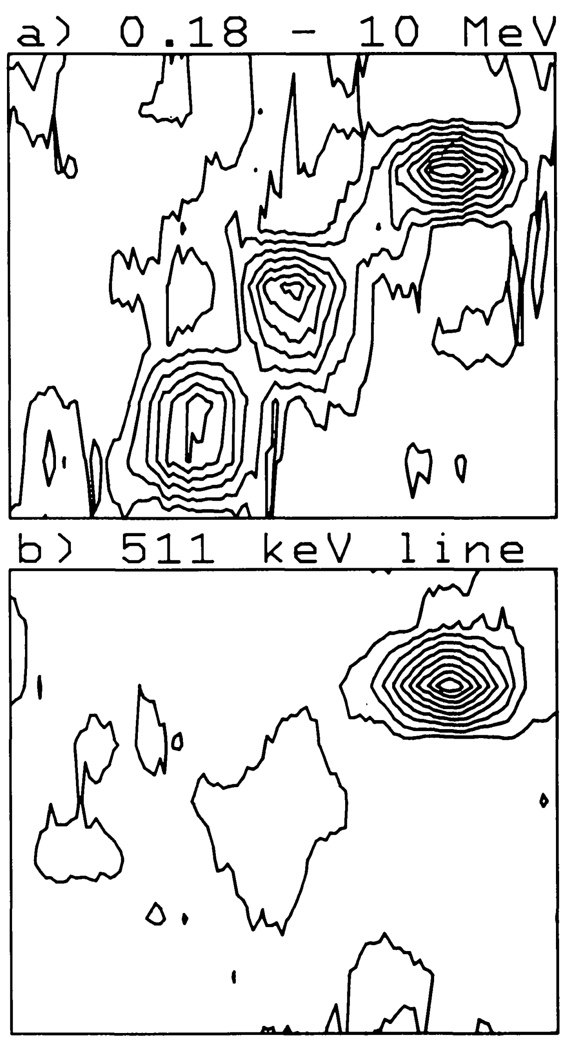

Fig. 5.6. Contour maps of simulated observations with the ZEBRA telescope of the galactic centre region in two energy bands.

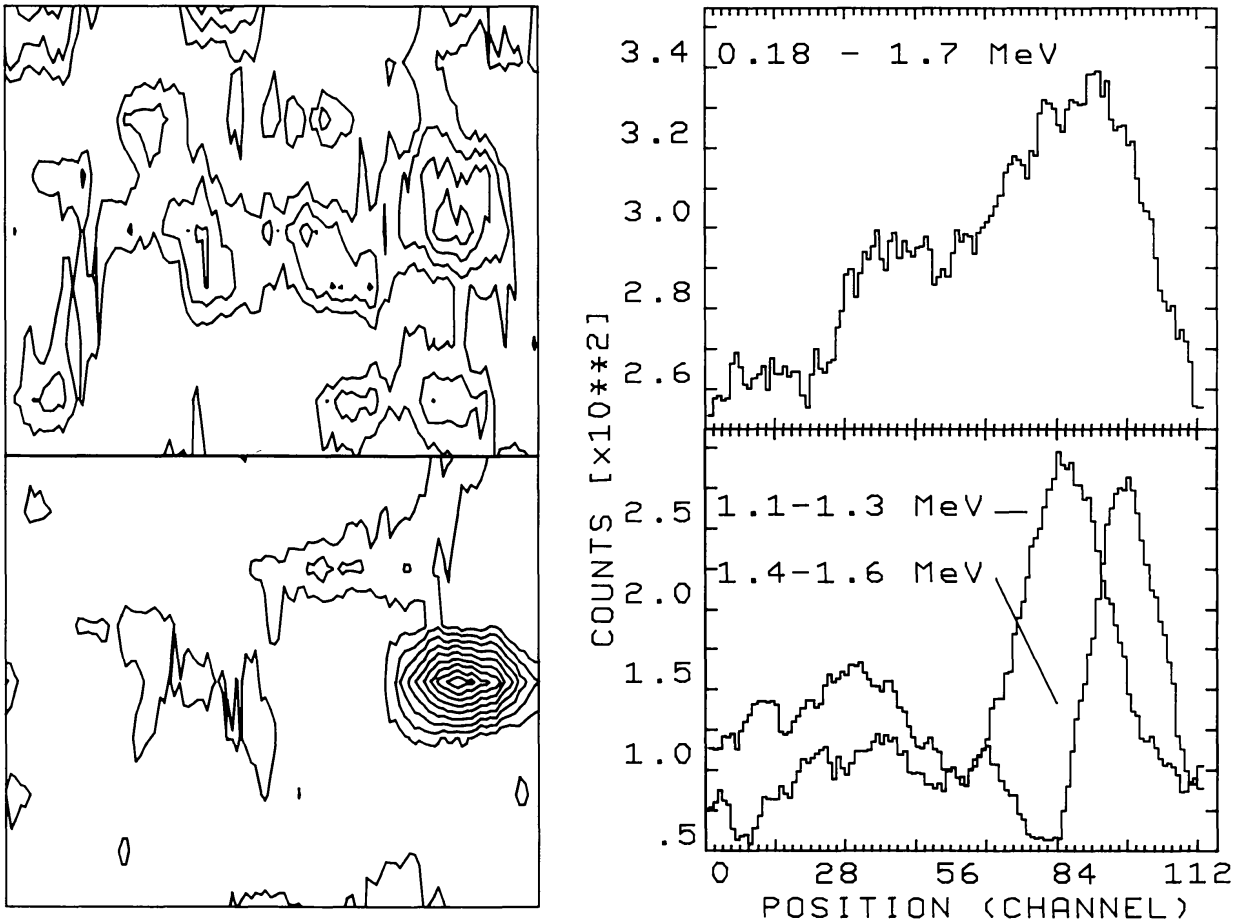

Fig. 5.7. Results from simulated observations with the ZEBRA telescope of SS433. On the left are contour maps for the spectral ranges 0.18–1.7 MeV (*upper*) and 1.4–1.6 MeV (*lower*), while on the right are cuts across the centres of the deconvolved images.

high-energy emitting regions are shown, obtained using a Monte Carlo code developed for simulation of imaging γ-ray telescopes having a rectangular geometry (Natalucci *et al.*, 1986; Stephen *et al.*, 1987a) for both the mask and the scintillation detector.

A similar design has been proposed for the European Recoverable Carrier (EURECA) platform constructed for use with the Space Shuttle (Eureca Flight Study, 1986). Two of the three instruments on board would be coded aperture devices covering the energy range from 10 keV–10 MeV. Unfortunately this proposal did not get beyond the preflight study phase, but it has since been mentioned in terms of the Space Station along with other, more exotic designs involving extendable masks (and hence a 'zoom' capability) (Carter *et al.*, 1986).

A further example of a coded-mask telescope in high energy astronomy is the Gamma-Ray Imaging Spectrometer (GRIS) (Figure 5.8). This telescope is designed to operate in the range 0.02–10 MeV and is particularly optimized for the study of the 511 keV annihilation line in the galactic centre region (Teegarden *et al.*, 1985). In order to reduce the 511 keV background induced by interactions in the mask material this design incroporates an active mask whose elements are 6.8 cm square NaI crystals of

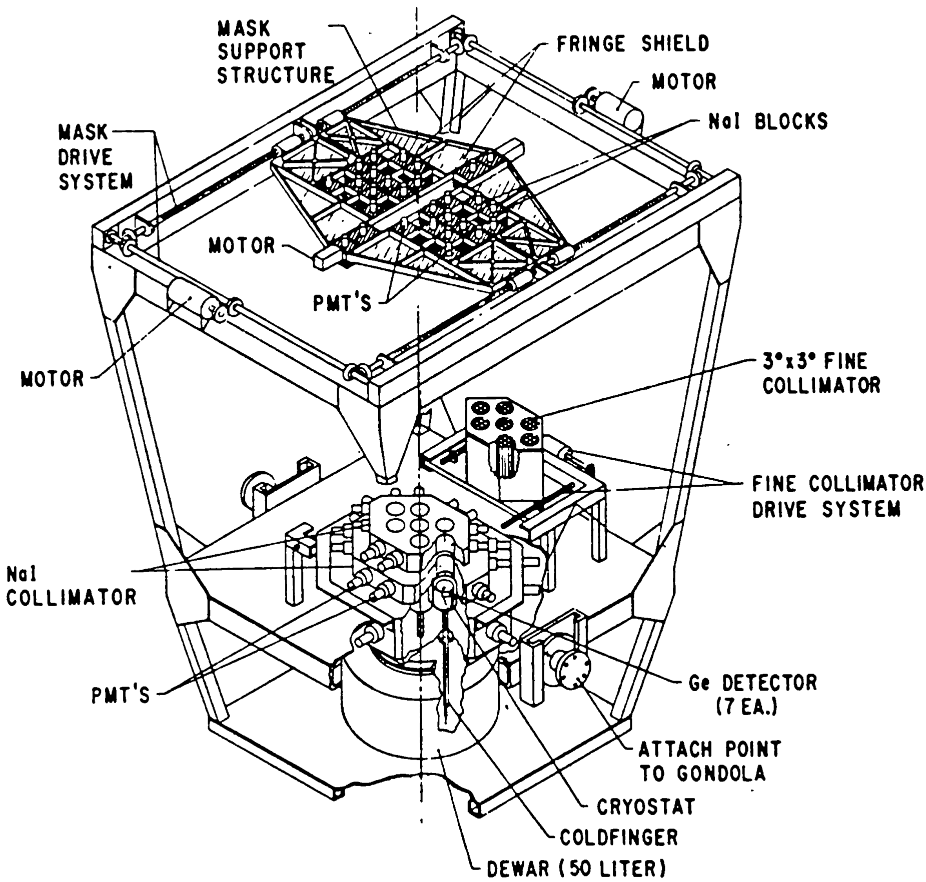

Fig. 5.8. Schematic view of GRIS (Teegarden *et al.*, 1985).

7.6 cm thickness. The mask is a 3 × 5 Hadamard URA with each solid element coupled to a photomultiplier tube and connected to the veto system of the telescope. A similarity to the (first) DGT design is the use of a mask/anti-mask system to eliminate background non-uniformity problems. To avoid the mechanical complexity and expense of constructing and accomodating two masks, a solution has been found in which the mask itself can be converted onto its own antimask by a simple movement of its elements (Figure 5.9). The GRIS instrument is an array of seven coaxial *n*-type germanium detectors (6.5 cm diameter, 6.5 cm thickness) surrounded by a thick active NaI shield/collimator. In order to produce a complete sky map (3 × 5 pixels) the mask/anti-mask system moves laterally so that a detector is located under each of the 15 basic pattern element at least once (Gehrels *et al.*, 1985). The mask-detector separation of 150 cm and the mask element size guarantee an angular resolution (FWHM) of 4° in both directions within a FCFV of 9° × 15°. The foreseen source location accuracy for the 511 keV line is ±0.2°.

Even at the highest energies (from 10 to ≈ 1000 MeV) plans exist for the use of coded aperture devices (Carter *et al.*, 1982b). Until now the feasiblity of an instrument working in this energy range has been studied with two different prototypes in laboratory experiments (Carter *et al.*, 1983; Jenkins *et al.*, 1985). The proposed telescope arrange-

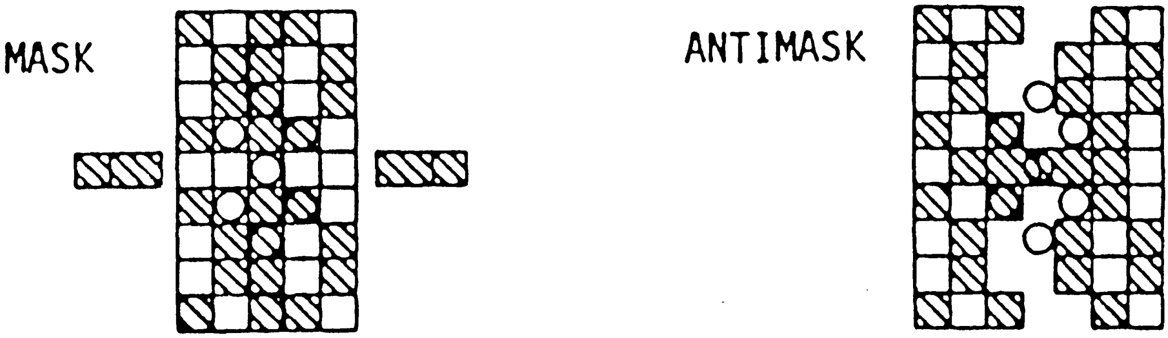

Fig. 5.9. GRIS mask to anti-mask conversion: the mask divides into halves while two independent elements rotate into the centre (Gehrels *et al.*, 1985).

ment consists of a passive mask (3 × 3 replication of a 29 × 31 quadratic residues pattern) made of 1.35 thick lead-antimony alloy and placed at 125 cm in front of the PSD. The detector consists of a drift chamber with a geometric area of 85 × 85 cm^2. Several accelerator tests have demonstrated the ability to reconstruct images of high-energy gamma-ray point sources (up to 120 MeV) with an angular resolution of the order of 0.2° and a point source location accuracy of a few arc min (Jenkins *et al.*, 1984).

5.6. Hexagonal URA's (HURA)

The California Institute group have recently constructed and flown a coded aperture telescope using an Hexagonal URA and operating in the hard X- and soft gamma-ray range (0.03–5 MeV) (Cook *et al.*, 1984): the Gamma-Ray Imaging Payload (GRIP). This imaging telescope consists of a NaI Anger camera associated with a rotating HURA (Figure 5.10). The primary detector is a 5 cm thick NaI crystal of 41 cm diameter read by an array of 19 PM tubes. For this scintillator thickness PM signals have a marked dependence on the depth of the γ-ray interaction, so to optimize the positional response of the detector, the authors have used, a 3-D algorithm based on the maximum likelihood method that permits a spatial resolution less than 1 cm (FWHM) over the range 0.1–5 MeV (Cook *et al.*, 1985). The PSD is actively shielded at the sides by 12 plastic scintillators forming a cylinder around the detector, and from below by a secondary Anger camera. The mask is situated 250 cm above the detector supported by an Al honeycomb sandwich and contains about 2000 hexagonal cells of 2 cm lead with an inner diameter of 2.5 cm (Althouse *et al.*, 1985). The fully-coded field of view of GRIP is about 20° with 0.6° geometric angular resolution, while the quoted point source location accuracy is ≈ 3 arc min at 10σ. The continuous rotation of the HURA mask guarantees that the reconstructed image is non-ambiguous even though the aperture contains several cycles of the basic (length 79) pattern in each direction (Figure 5.11). The flight took place on 15–16 October, 1985 from Palestine, Texas, during which observations of the Crab supernova remnant, the quasar 3C273, the galactic anti-centre and the Cygnus region were carried out. The data analysis is still in progress, nevertheless flux maps of the Crab and Cygnus X-1 regions have been

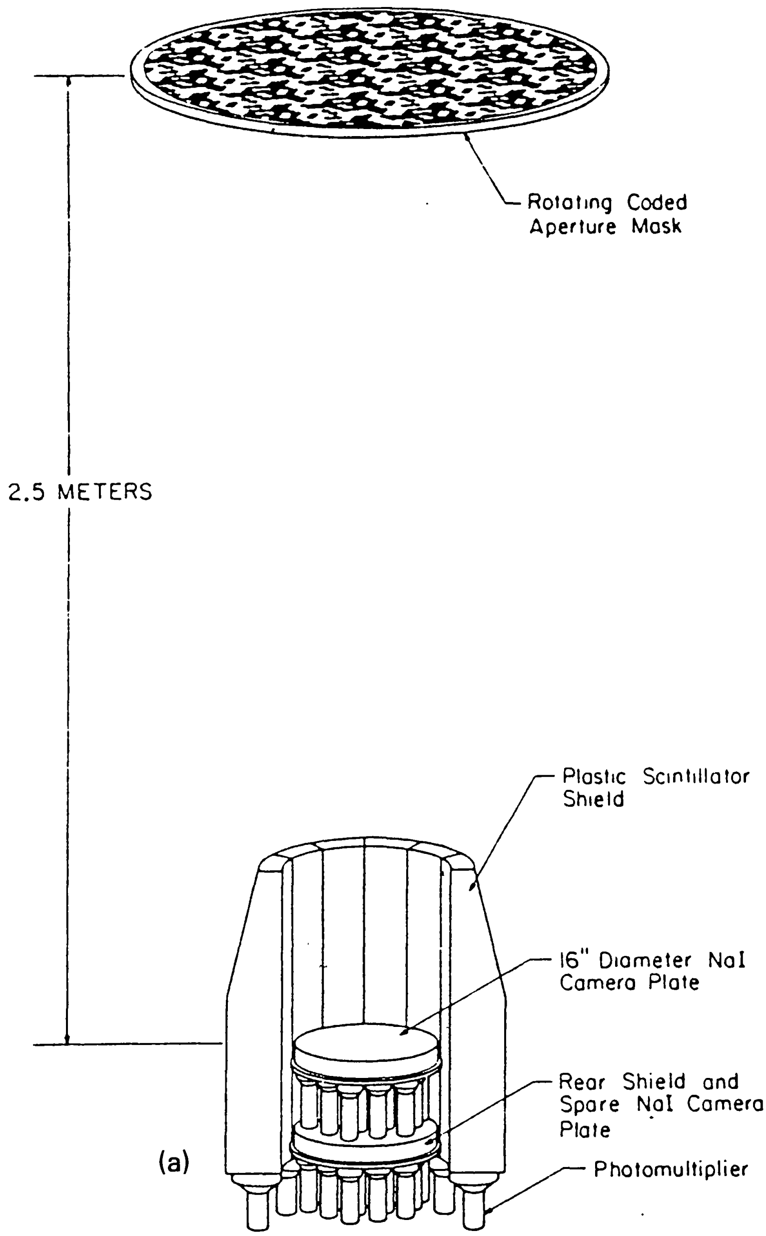

Fig. 5.10. The Gamma-Ray Imaging Payload (GRIP): (a) basic elements of the telescope; (b) mask pattern (Althouse *et al.*, 1985).

obtained already showing a 13 and 19σ significance level, respectively, over the energy range 50–150 keV (Althouse *et al.*, 1987).

The GRASP satellite, now accepted for the phase A study by the European Space Agency (ESA), is based on the coded aperture technique and has been conceived as a major step forward in gamma-ray astronomy (0.015–100 MeV). At the end of the assessment study (Grasp Assessment Study, 1986) it consists of a two-part detection plane – a central region of 900 cm^2 solid state germanium detectors providing very high spectral resolution, surrounded by 3300 cm^2 of CsI (Tl) position sensitive scintillation elements, arranged in a square format. Although the use of a rectangular mask has been considered (Bignami *et al.*, 1987) according to a more recent suggestion the PSD may

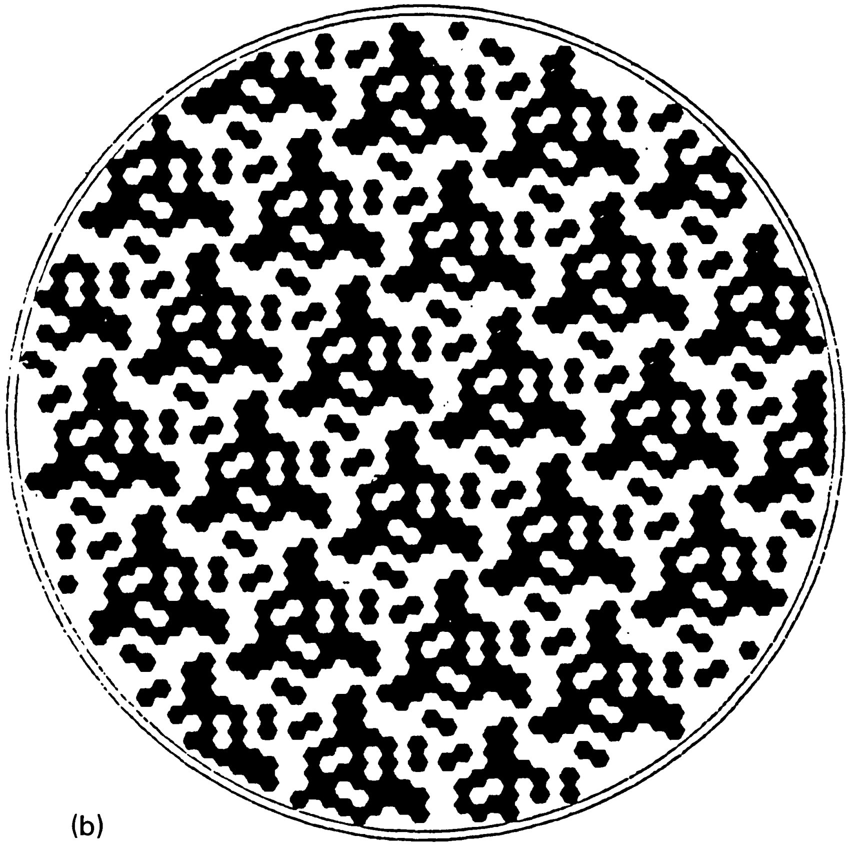

(b)

Fig. 5.10b.

be arranged in a hexagonal/circular pattern so as to make it more suitable for use with a rotating HURA. At the moment both the mask pattern and the overall geometric configuration are still to be fixed. Possible instrumental characteristics are detailed in Table I.

(a)

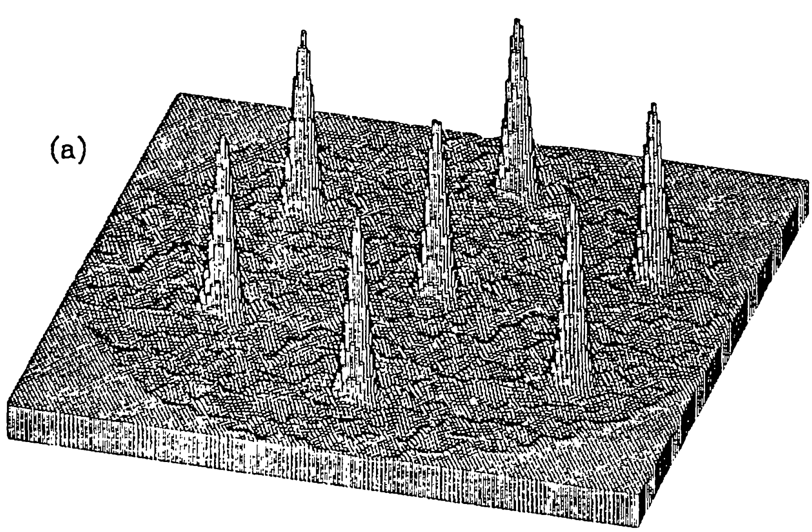

Fig. 5.11. (a) Ambiguous image of a single point source obtained with an extended HURA which was not continuously rotated; (b) Image obtained with a continuously rotated HURA; (c) The image after ring removal (Cook *et al.*, 1984).

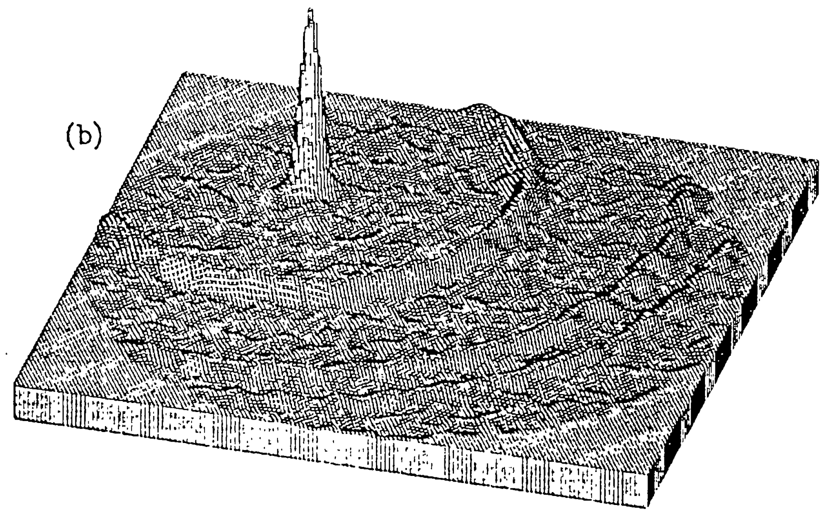

Fig. 5.11b.

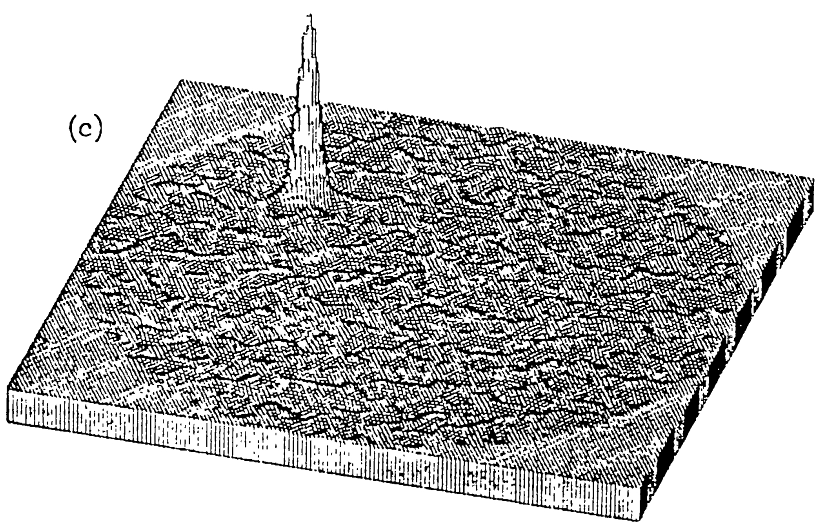

Fig. 5.11c.

6. Conclusions

As in other branches of astronomy, imaging instrumentation plays an essential role in increasing our understanding of X- and γ-ray astrophysical phenomena. In this spectral range coded aperture imaging has proven to be an efficient method for mapping and monitoring selected regions of the sky. It offers the advantage of combining a wide field of view with good angular resolution and efficiency.

Of particular importance is the role played by this technique in the regime of low-energy gamma-ray astronomy – a domain in which observations have suffered from the marginal sensitivity of the first effective generation of telescopes where, in order to provide directionality, massive shielding was employed at the expense of collecting area. On the other hand, the so-called double Compton instruments have not so far achieved a high sensitivity coupled with an angular resolution better than a few degrees. The coded aperture imaging technique makes unnecessary the use of bulk shielding systems, which are themselves a source of local background, allowing the construction of large sensitive area detectors with high-angular resolution and a field of view adequate for the study of crowded γ-ray sky regions. Furthermore, as the source and background measurements are spatially multiplexed, background subtraction can be performed on a continuous basis, avoiding biases in source flux evaluations due to temporal background variations. Even at higher energies, coded mask systems will be employed on the Gamma-1 satellite and other experiments in order to increase the angular resolution obtainable although some doubt has been expressed that the decrease in effective area caused by the presence of the mask may aggravate the problem of very low statistical significance observations.

The wide range of mask patterns available allows flexibility in instrument design and relative ease of manufacturing, thus providing an advantage over other imaging methods such as grazing incidence or Compton telescopes. This explains why a large number of mask-based detector systems have flourished in a relatively short period and why many more experiments are planned for the near future.

As underlined in this paper, theoretical aspects are of great importance, as the analysis of the data obtained from these instruments includes a large amount of digital image processing and restoration, which can only be correctly applied once a detailed and accurate understanding of the encoding/decoding steps is achieved. On the other hand, the historical review presented here details of the increasingly sophisticated refinements of the coded imaging approach which have taken place over the last two decades and illustrates the potential for further developments in this exciting field of instrumental X- and γ-ray astronomy.

Acknowledgements

The authors would like to thank the ever-increasing number of workers in the field of coded aperture imaging for supplying the vast amount of literature on the subject, and to apologise in advance for any inadvertent omissions in the bibliography.

References

Ables, J. G.: 1968, *Proc. Astron. Soc. Australia* **1**, 172.

Aitken, G. J. M., Corteggiani, J. P., and Gay, J.: 1981, *J. Opt. Soc. Am.* **71**, 759.

Akimov, V. V., Nesterov, V. E., Kalinkin, L. F., Balibanov, V. M., Prilutsky, O. F., Rodin, V. R., Leikov, N. G., Bielaoussov, A. S., Dobrian, L. B., Poluetkov, V. P., Gerassimov, I. A., Koslov, V. D., Voronov, S. A., Galper, A. M., Kirrilov-Ugriumov, V. G., Oseroy, Y. V., Grigoriev, V. A., Iaurkine, Y. T., Popov, A. V., Kurnosova, L. V., Fradkin, M. N., Tsuikin, E. I., Leray, J. P., Gros, M., Parlier, B., Soroka, F., Masse, P., Bazer-Bachi, A. R., and Lavigne, J. M.: 1985, *Proc. 19th Int. Cosmic Ray Conf., La Jolla (U.S.A.)*, OG 9.2–10, p. 330.

Althouse, W. E., Cook, W. R., Cummings, A. C., Finger, M. H., Prince, T. A., Schindler, S. M., Starr, C. H., and Stone, E. C.: 1985, *Proc. 19th Int. Cosmic Ray Conf.*, La Jolla (U.S.A.), OG 9.2–2, p. 299.

Althouse, W. E., Cook, W. R., Cummings, A. C., Finger, M. H., Palmer, D. M., Prince, T. A., Schindler, S. M., Starr, C. H., and Stone, E. C.: 1987, *Proc. 20th Int. Cosmic Ray Conf., Moscow (U.S.S.R.)*, OG 2.1–12 (in press).

Andrews, H. C. and Hunt, B. R.: 1977, *Digital Image Restoration*, Prentice Hall, Inc., New Jersey.
Aschenbach, B.: 1985, *Rep. Progr. Phys.* **48**, 579.
Badiali, M., Cardini, D., Emanuele, A., and Ranieri, M.: 1982, Internal Report No. 17, Istituto di Astrofisica Spaziale, Frascati, Italy.
Badiali, M., Cardini, D., Emanuele, A., Ranieri, M., and Soggiu, E.: 1985, *Astron. Astrophys.* **151**, 259.
Baker, R. E., Barbareschi, L., Bazzano, A., Butler, R. C., Caroli, E., Carter, J. N., Catani, O., Charalambous, P., Court, A. J., Di Cocco, G., Igiuni, A., La Padula, C., Morelli, E., Polcaro, F., Ramsden, D., Rubini, A., Santini, M., Spada, G., Traci, A., Ubertini, P., and Villa, G.: 1983a, *Adv. Space Res.* **3**, 95.
Baker, R. E., Charalambous, P. M., Dean, A. J., Drane, M., Gil, A., Stephen, J. B., Barbareschi, L., Boella, G., Bussini, A., Perotti, F., Villa, G., Butler, C., Caroli, E., Di Cocco, G., Morelli, E., Spizzichino, A., Badiali, M., Bazzano, A., La Padula, C., Polcaro, F., and Ubertini, P.: 1983b, *Proc. 18th Int. Cosmic Ray Conf., Bangalore (India)* **8**, 11.
Barrett, H. H. and DeMeester, G. D.: 1974, *Appl. Optics* **13**, 1100.
Barrett, H. H. and Horrigan, F. A.: 1973, *Appl. Optics* **12**, 2686.
Barrett, H. H., Stoner, W. W., Wilson, D. T., and DeMeester, G. D.: 1974, *Opt. Eng.* **13**, 539.
Baumert, L. D.: 1969, *SIAM J. Appl. Math.* **17**, 826.
Baumert, L. D.: 1971, 'Cyclic Difference Sets', *Lecture Notes in Maths.*, Springer-Verlag, Berlin, p. 182.
Bazer-Bachi, R., Cottin, F., Lavigne, J. M., Mandrou, P., Akimov, V., Dobriyan, M., Fradkin, M., Kalinkin, L., Nesterov, V., Tabaldeiev, S., Galper, A., Grigoriev, V., Kirillov-Ugryumov, V., Lutchkov, B., Ozerov, Y., Voronov, S., Tchuikin, E., Cretolle, J., Gros, M., Hugot, C., Keirle, P., Leray, J. P., Paul, J. A., and Raviart, A.: 1977, *Proc. 12th ESLAB Symp., Frascati, Italy*, ESA SP-124, 269.
Bignami, G. F., Boella, G., Burger, J. J., Keirle, P., Mayer Hasselwander, H. A., Paul, J. A., Pfefferman, E., Scarsi, L., Swanenburg, B. N., Taylor, B. G., Voges, W., and Wills, R. D.: 1975, *Space Sci. Instr.* **1**, 245.
Bignami, G. F., Dean, A. J., Durouchoux, Ph., Lund, N., McBreen, B., Ramsden, D., Staubert, R., Taylor, B. G., and Vedrenne, G.: 1987, *IEEE Trans. Nucl. Sci.* **NS-34**, 31.
Blake, R. L., Burek, A. J., Fenimore, E., and Puetter, R.: 1974, *Rev. Sci. Instr.* **45**, 513.
Boella, G., Bussini, A., Butler, R. C., Caroli, E., Charalambous, P. M., Dean, A. J., Di Cocco, G., Donati, S., Graham, G., Holder, S. M., Mastropietro, M., Perotti, F., Santambrogio, R., Traci, S., Ubertini, P., Villa, G., and Younis, F. A.: 1986, *IEEE Trans. Nucl. Sci.* **33**, 755.
Boyd, R. L. F.: 1973, *Quart. J. Roy. Astron. Soc.* **14**, 218.
Bradt, H., Garmire, G., Oda, M., Spada, G., Sreekantan, V., Gorenstein, P., and Gursky, H.: 1968, *Space Sci. Rev.* **8**, 471.
Brinkman, A. C., Dam, J., Mels, W. A., Skinner, G. K., and Willmore, W. P.: 1983, in G. C. Perola and M. Salvati (eds.), *Proc. of the International Workshop 'Non-Thermal and Very High-Temperature Phenomena in X-ray Astronomy*, Rome (Italy), 263.
Brown, C.: 1974, *J. Appl. Phys.* **45**, 1806.
Brown, T. M.: 1978, *J. Opt. Soc. Am.* **68**, No. 7, 883.
Butler, R. C., Caroli, E., Di Cocco, G., Maggioli, P. P., Spizzichino, A., Charalambous, P. M., Dean, A. J., Drane, M., Gil, A., Stephen, J. B., Perotti, F., Villa, G., Badiali, M., La Padula, C., Polcaro, F., and Ubertini, P.: 1984, *Nucl. Instr. Meth. Phys. Res.* **221**, 41.
Butler, R. C., Caroli, E., Di Cocco, G., Natalucci, L., Spada, G., Spizzichino, A., Stephen, J. B., Carter, J. N., Charalambous, P. M., Dean, A. J., Graham, G., Maggioli, P., Young, N. G. S., Younis, F., Boella, G., Perotti, F., Villa, G., La Padula, C., and Ubertini, P.: 1985, *Proc. 19th Int. Cosmic Ray Conf., La Jolla (U.S.A.)* **3**, 322.
Byrnak, B. P., Christensen, E. F., Westergaard, N. J., and Schnopper, H. W.: 1985, *Appl. Optics* **24**, 2543.
Cannon, T. M. and Fenimore, E. E.: 1979, *Appl. Optics* **18**, 1979.
Cannon, T. M. and Fenimore, E. E.: 1980, *Opt. Eng.* **19**, 283.
Cardini, D., Badiali, M., Emanuele, A., Farina, G., Gianni, G., Ranieri, M., Catanesi, M. G., Maggi, G., Selvaggi, G., and Waldner, F.: 1983, *Astron. Astrophys.* **127**, 169.
Caroli, E., Butler, R. C., Di Cocco, G., Maggioli, P. P., Natalucci, L., and Spizzichino, A.: 1984, *Nuovo Cimento* **7C**, 786.
Carter, J. N., Ramsden, D., Frye, G. M., Jr., Jenkins, T. L., and Koga, R.: 1982, *Monthly Notices Roy. Astron. Soc.* **198**, 33.
Carter, J. N., Frye, G., Hall, C. J., Jenkins, T. L., Owen, A., and Ramsden, D.: 1983, *Adv. Space Res.* **3**, 49.
Carter, J. N., Coe, M. J., Dean, A. J., and Ramsden, D.: 1986, *J. British Interplanetary Soc.* **39**, 366.

Ceglio, N. M., Attwood, D. T., and George, E. V.: 1977, *J. Appl. Phys.* **48**, 1566.

Chang, L. T., MacDonald, B., Perez-Mendez, V., and Shiraishi, L.: 1975, *IEEE Trans. Nucl. Sci.* **NS-22**, 374.

Charalambous, P. M., Dean, A. J., Stephen, J. B., and Young, N. G. S.: 1984a, *Appl. Optics* **23**, 4118.

Charalambous, P. M., Dean, A. J., Drane, M., Gil, A., Stephen, J. B., Young, N. G. S., Butler, R. C., Caroli, E., Di Cocco, G., Spada, G., Spizzichino, A., Barbareschi, L., Perotti, F., Villa, G., Badiali, M., La Padula, C., Polcaro, F., and Ubertini, P.: 1984b, *Nucl. Instr. Meth. Phys. Res.* **221**, 183.

Chou, C. and Barrett, H. H.: 1978, *Opt. Letters* **3**, 187.

Cook, W. R., Finger, M., Prince, T. A., and Stone, E. C.: 1984, *IEE Trans. Nucl. Sci.* **NS-31**, 771.

Cook, W. R., Finger, M., and Prince, T. A.: 1985, *IEEE Trans. Nucl. Sci.* **NS-32**, 129.

Crannel, H. and Maurer, G. S.: 1977, *Proc. 12th ESLAB Symp., Frascati, Italy*, ESA SP-124, 243.

Daniell, G. J.: 1984, *Nucl. Instr. Meth. Phys. Res.* **221**, 67.

Debouzy, G.: 1983, *Adv. Space Res.* **3**, 99.

De Chiara, P. and Frontera, F.: 1987, in C. Castagnoli (ed.), *Proc. 3rd National Symp. on Space Physics, Saint Vincent (Italy)*, Compositori Publ., Bologna, p. 255.

De Jager, C.: 1974, *Astrophys. Space Sci* **31**, 417.

Derdeyn, S. M., Ehrmann, C. H., Fichtel, C. E., Kniffen, D. A., and Ross, R. W.: 1972, *Nucl. Instr. Methods* **98**, 557.

Dicke, R. H.: 1968, *Astrophys. J.* **153**, L101.

Di Cocco, G.: 1986, *Proc. 15th Int. Symp. on Space Sci. and Tech., Tokyo (Japan)* **2**, 1879.

Ducros, G. and Ducros, R.: 1984, *Nucl. Instr. Meth. Phys. Res.* **A221**, 49.

Durouchoux, P., Hudson, H., Hurford, G., Hurley, K., Matteson, J., and Orsal, E.: 1983, *Astron. Astrophys.* **120**, 150.

Emanuele, A., Badiali, M., Cardini, D., Ranieri, M., Catanesi, M. G., Maggi, G., Selvaggi, G., and Waldner, F.: 1984, *Astron. Astrophys.* **132**, 33.

Eyles, C. J., Skinner, G. K., Willmore, A. P., Bertram, D., Harper, P. K. S., Herring, J. R. H., and Ponman, T. J.: 1987, *J. British Interplanetary Soc.* **40**, 159.

EURECA Reflight Study: 1986, *Executive Summary*, MBB-ERNO.

Fenimore, E. E.: 1978, *Appl. Optics* **17**, 3562.

Fenimore, E. E.: 1980, *Appl. Optics* **19**, 2465.

Fenimore, E. E.: 1983, *Appl. Optics* **22**, 826.

Fenimore, E. E. and Cannon, T. M.: 1978, *Appl. Optics* **17**, 337.

Fenimore, E. E. and Weston, G. S.: 1981, *Appl. Optics* **20**, 3058.

Fenimore, E. E. and Cannon, T. M., Van Hulsteyn, D. B., and Lee, P.: 1979, *Appl. Optics* **18**, 945.

Fichtel, C. E., Bertsch, D. L., Hartman, R. C., Kniffen, D. A., Thompson, D. J., Hofstadter, R., Hughes, E. B., Campbell-Finmann, L. E., Pinkau, K., Mayer-Hasselwander, H., Kanbach, G., Rothermel, H., Sommer, M., Favale, A. J., and Schneid, E. J.: 1983, *Proc. 18th Int. Cosmic Ray Conf., Bangalore (India)* **8**, 19.

Finger, M. H. and Prince, T. A.: 1985, *Proc. 19th Int. Cosmic Ray Conf., La Jolla (U.S.A.)*, OG 9.2–1, 295.

Fischer, A. G.: 1967, *SIAM J. Appl. Math.* **15**, 269.

Fleming, J. S. and Goddard, B. A.: 1984, *Nucl. Instr. Meth. Phys. Res.* **221**, 242.

Frontera, F., Dal Fiume, D., Franceschini, T., Landini, G., Morelli, E., Pamini, M., Rubini, A., Silvestri, S., Spada, G., Costa, E., Cardini, D., and Emanuele, A.: 1984, *Nuovo Cimento* **7C**, 656.

Garcia, M. R., Grindlay, J. E., Burg, R., Murray, S. S., and Flanagan, J.: 1986, *IEEE Trans. Nucl. Sci.* **33**, 735.

Gehrels, N., Cline, T. L., Huters, A. F., Leventhal, M., MacCallum, C. J., Reber, J. D., Stang, P. D., Teegarden, B. J., and Tueller, J.: 1985, *Proc. 19th Int. Cosmic Ray Conf., La Jolla (U.S.A.)*, OG 9.2–3, 303.

Giles, A. B.: 1981, *Appl. Optics* **20**, 3068.

Golay, M. J. E.: 1971, *J. Opt. Soc. Am.* **61**, 272.

Gottesman, S. R. and Schneid, E. J.: 1986, *IEEE Trans. Nucl. Sci.* **33**, 745.

Gourlay, A. R. and Stephen, J. B.: 1983, *Appl. Optics* **22**, 4042.

Gourlay, A. R. and Young, N. G.: 1984, *Appl. Optics* **23**, 4111.

Gourlay, A. R., Stephen, J. B., and Young, N. G. S.: 1984, *Nucl. Instr. Meth. Phys. Res.* **221**, 54.

Grindlay, J. E., Garcia, M. R., Burg, R. I., and Murray, S. S.: 1986, *IEEE Trans. Nucl. Sci.* **33**, 750.

Grindlay, J. E. and Murray, S. S.: 1981, *Proc. of the Workshop*, No. 349.

Gunson, J. and Polychronopulos, B.: 1976, *Monthly Notices Roy. Astron. Soc.* **177**, 485.

Graffstein, A.: 1975, *Nucl. Instr. Meth.* **131**, 173.
GRASP Assessment Study: 1986, ESA SCI(86)4.
Groh, G., Hayat, G. S., and Stroke, G. W.: 1972, *Appl. Optics* **11**, 931.
Hall, M., Jr.: 1967, *Combinatorial Theory*, Blaisdell, Whaltam Publ., Massachusetts.
Hammersley, A. P.: 1986, Ph.D. Thesis, University of Birmingham.
Hammersley, A. P. and Skinner, G. K.: 1984, *Nucl. Instr. Meth.* **221**, 45.
Harper, P. K. S., Skinner, G. K., Eyles, C. J., Willmore, A. P., Bertram, D., Herring, J. R. H., Peden, J. C. M., Pollock, A. M. I., and Ponman, T. J.: 1987, *J. British Interplanetary Soc.* **40**, 163.
Hartman, R., Fichtel, C., Kniffen, D., Stacy, G., and Trombka, J.: 1983, *Proc. 18th Int. Cosmic Ray Conf., Bangalore (India)* **8**, 16.
Harwit, M. and Sloane, N. J. A.: 1979, *Hadamard Transform Optics*, Academic Press, New York, San Francisco, London.
Harwit, M., Phillips, P. G., King, L. W., and Briotta, D., Jr.: 1974, *Appl. Optics* **13**, 2669.
Helmken, H., Gorenstein, P., and Gursky, H.: 1975, *Proc. 14th Int. Cosmic Ray Conf., München (Germany)* **9**, 3111.
Holt, S. S.: 1976, *Astrophys. Space Sci.* **42**, 123.
Holt, S. S. and Priedhorsky, W.: 1986, *Bull. Am. Astron. Soc.* **17**, 848.
Holt, S. S., Boldt, E. A., Serlemitsos, P. J., and Kaluzienski, L. J.: 1976, *Astrophys. J.* **203**, L63.
Horstman, H. M., Camprini, M., Giovannini, G., Poulsen, J. M., Sassi, D., and Ventura, G.: 1984, TESRE/CNR Technical Report No. 101.
Huang, T. S., and Narendra, P. M.: 1975, *Appl. Optics* **14**, 2213.
Jenkins, T. L., Frye, G. M., Jr., Owens, A., Carter, J. N., and Ramsden, D.: 1984, *Nucl. Instr. Meth.* **221**, 278.
Jenkins, T. L., Frye, G. M., Jr., Hall, C. J., Owens, A., Pendleton, G. N., Carter, J. N., Ramsden, D., Agrinier, B., Bonfand, E., Refloch, A., and Tabary, A.: 1985, *Proc. 19th Int. Cosmic Ray Conf.*, OG 9.2–7, Proc. of the Workshop.
Johansson, A., Beron, B. L., Campbell, L., Eichler, R., Gorodetsky, P., Hofstadter, R., Hughes, E. B., and Wilson, S.: 1980, *IEEE Trans. Nucl. Sci.* **NS-27**, 375.
Johnsen, E. C.: 1966, *J. Algebra* **4**, 388.
Knoll, G. F., Rogers, W. L., Koral, K. F., Stamos, J. A., and Clinthorne, N. H.: 1984, *Nucl. Instr. Methods Phys. Res.* **A221**, 226.
Laub, B. and Reinhardt, E. R.: 1983, in H. W. Schussler (ed.), *Signal Processing II: Theories and Applications*, Elsevier Science Publ. B.V., North-Holland, p. 593.
Lempel, A.: 1979, *Appl. Optics* **18**, 4064.
Lund, N.: 1986a, in J. L. Culhane (ed.), *SPIE Proc. on 'X-ray Instrumentation in Astronomy'*, No. 597.
Lund, N.: 1986b, in J. L. Culhane (ed.), *SPIE Proc. on 'X-ray Instrumentation in Astronomy'*, No. 597.
MacWilliams, F. J. and Sloane, N. J. A.: 1976, *Proc. IEEE* **64**, 1715.
Maeda, J. and Murata, K.: 1984, *Appl. Optics* **83**, 857.
Maggioli, P. P., Caroli, E., Natalucci, L., Spizzichino, A., and Badiali, M.: 1984, *Nucl. Instr. Meth. Phys. Res.* **A221**, 82.
Mandrou, P.: 1984, *Adv. Space Res.* **3**, 525.
McConnell, M. L., Forrest, D. J., Chupp, E. L., and Dunphy, P. P.: 1982, *IEEE Trans. Nucl. Sci.* **NS-29**, 155.
McConnell, M. L., Dunphy, P. P., Forrest, D. J., and Chupp, E. L.: 1983, *Adv. Space Res.* **3**, 105.
McConnell, M. L., Chupp, E. L., Dunphy, P. P., Forrest, D. J., and Owens, A.: 1987a, *Proc. 20th Int. Cosmic Ray Conf., Moscow (U.S.S.R.)*, OG 9.1–9 (in press).
McConnell, M. L., Owens, A., Chupp, E. L., Dunphy, P. P., Forrest, D. J., and Vestrand, W. T.: 1987b, *Proc. 20th Int. Cosmic Ray Conf., Moscow (U.S.S.R.)*, OG 2.1–4 (in press).
McConnell, M. L., Chupp, E. L., Dunphy, P. P., Forrest, D. J., and Owens, A.: 1987c, *Proc. 20th Int. Cosmic Ray Conf., Moscow (U.S.S.R.)*, OG 2.1–6 (in press).
McConnell, M. L., Dunphy, P. P., Forrest, D. J., Chupp, E. L., and Owens, A.: 1987d, *Astrophys. J.* (in press).
McKechnie, S. P., Bennett, K., and Ramsden, D.: 1977, *Proc. 15th Int. Cosmic Ray Conf., Plodiv (Bulgaria)* **8**, 11.
Mertz, L. and Young, N. O.: 1961, *Proc. Int. Conf. on Opt. Instr. Tech.*, Chapman and Hall, London, p. 305.
Miyamoto, S.: 1977, *Space Sci. Instr.* **3**, 473.
Miyamoto, S., Tsunemi, H., and Tsuno, K.: 1981, *Nucl. Instr. Meth.* **180**, 557.

Natalucci, L., Spizzichino, A., Di Cocco, G., Butler, R. C., Caroli, E., and Stephen, J. B.: 1986, *Proc. 2nd European Simulation Congress, Antwerp (Belgium)*, p. 484.

Ohyama, N., Endo, T., Honda, T., Tsujiuchi, J., Matumoto, T., Iinuma, T., and Ishimatsu, K.: 1984, *Appl. Optics* **23**, 3168.

Oliver, C. J.: 1976, *Appl. Optics* **15**, 93.

Owens, A., Frye, G. M., Hall, C. J., Jenkins, T. L., Pendleton, G. N., Carter, J. N., Ramsden, D., Agrinier, B., Bonfand, E., Gouiffes, C., and Tabary, A.: 1985, *Proc. 19th Int. Cosmic Ray Conf., La Jolla (U.S.A.)*, OG 9.2–6, p. 314.

Owens, A., Bhattacharya, D., Chupp, E. L., Dunphy, P. P., Forrest, D. J., and McConnell, M. L.: 1987, *Proc. 20th Int. Cosmic Ray Conf., Moscow (U.S.S.R.)*, OG 2.3–13 (in press).

Palmieri, T. M.: 1974, *Astrophys. Space Sci.* **20**, 431.

Parlier, B., Agrinier, B., Bonfand, E., Mougin, E., Lecomte, A., Andrejol, J., Curtois, J. C., Lavigne, J. M., Niel, M., Vedrenne, G., and Doulade, C.: 1977, *Proc. 12th ESLAB Symp., Frascati, Italy*, ESA SP-124, 257.

Palmer, D. and Prince, A.: 1987, *IEEE Trans. Nucl. Sci.* **NS-34**, 71.

Penrose, R.: 1955, *Proc. Cambridge Philos. Soc.* **41**, 406.

Plankey, F. W., Glenn, T. H., Hart, L. P., and Winefordner, J. D.: 1974, *Analyt. Chem.* **46**, 1000.

Pratt, W. K.: 1978, *Digital Image Processing*, John Wiley and Sons, New York.

Prilutsky, D. F.: 1979, *Proc. XXII IAU/COSPAR Symp. on 'Non-Solar-Ray Astronomy', Bangalore (India).*

Proctor, R. J.: 1981, in S. S. Holt (ed.), *Proc. Workshop 'X-Ray Astronomy in the 1980's*, Nasa Memorandum 83848, p. 335.

Proctor, R. J., Skinner, S. K., and Willmore, A. P.: 1978, *Monthly Notices Roy. Astron. Soc.* **185**, 745.

Proctor, R. J., Skinner, S. K., and Willmore, A. P.: 1979, *Monthly Notices Roy. Astron. Soc.* **187**, 633.

Ranieri, M., Badiali, M., Cardini, D., Emanuele, E., and Auriemma, C.: 1981, *J. British Interplanetary Soc.* **34**, 135.

Rocchia, R., Deschamps, J. Y., Koch-Miramond, L., and Tarrius, A.: 1985, *Workshop on 'Cosmic X-Ray Spectroscopy Mission'*, ESA SP-239, 277.

Scarsi, L.: 1984, *Adv. Space Res.* **3**, 491.

Schönfelder, V., Graser, U., and Diehl, R.: 1982, *Astron. Astrophys.* **110**, 138.

Schönfelder, V., Diehl, R., Lichti, G. G., Steinle, H., Swanenburg, B. N., Deerenberg, A. J. M., Aarts, H., Lockwood, J., Webber, W., Macri, J. Ryan, J., Simpson, G., Taylor, B. G., Bennett, K., and Snelling, M.: 1984, *IEEE Trans. Nucl. Sci.* **NS-31**, 766.

Schnopper, H. W. and Byrnak, B.: 1985, *Proc. ESA Workshop 'Cosmic X-Ray Spectroscopy Mission*, Lingby, Denmark, p. 283.

Simone, J., O'Neill, T., Tumer, O. T., and Zych, A. D.: 1985, *IEEE Trans. Nucl. Sci.* **NS-32**, 124.

Sims, M. R., Turner, M. J. L., and Willingale, R.: 1980, *Space Sci. Instr.* **5**, 109.

Sims, M. R., Willingale, R., and Turner, M. J. L.: 1984, *Nucl. Instr. Meth. Phys. Res.* **A221**, 77.

Sims, M. R., Turner, M. J. L., and Willingale, R.: 1985, *Nucl. Instr. Meth. Phys. Res.* **A228**, 512.

Singer, J.: 1938, *Trans. Am. Math. Soc.* **43**, 377.

Skinner, G. K.: 1980, *J. British Interplanetary Soc.* **33**, 333.

Skinner, G. K.: 1984, *Nucl. Instr. Meth.* **221**, 33.

Skinner, G. K., Eyles, C. J., and Willmore, A. P.: 1987, *Phys. Bull.* **38**, 10.

Sloane, N. J. A. and Harwit, M.: 1976, *Appl. Optics* **15**, 107.

Sloane, N. J. A., Fine, T., Phillips, P. G., and Harwit, M.: 1969, *Appl. Optics* **8**, 2103.

Spada, G.: 1983, in G. C. Perola and M. Salvati (eds.), *Proc. Internationaè Workshop 'Non-Thermal and Very High Temperature Phenomena in X-Ray Astronomy', Rome (Italy)*, p. 217.

Stephen, J. B., Caroli, E., Di Cocco, G., Maggioli, P. P., Natalucci, L., and Spizzichino, A.: 1987a, *Astron. Astrophys.* (in press).

Stephen, J. B., Bassani, L., Butler, R. C., Caroli, E., Di Cocco, G., Natalucci, L., and Spizzichino, A.: 1987b, in C. Castagnoli (ed.), *Proc. 3rd National Symp. on Space Physics, Saint Vincent (Italy)*, Compositori Publ., Bologna, p. 217.

Tanaka, Y.: 1984, *Adv. Space Res.* **3**, 509.

Tanaka, Y., Fujii, M., Inoue, H., Kawai, N., Koyama, K., Maejima, Y., Makino, F., Makishima, K., Matsuoka, M., Mitsuda, K., Murakami, T., Nishimura, J., Oda, M., Ogawara, Y., Ohashi, T., Shibazaki, N., Suzuki, K., Waki, I., Yamagami, T., Kondo, I., Murakami, H., Hayakawa, S., Hirano, T., Kunieda, H., Masai, K., Nagase, F., Sato, N., Tawara, Y., Kitamoto, S., Miyamoto, S., Tsunemi, H., Yamashita, K., and Nakagawa, M.: 1984, *Publ. Astron. Soc. Japan* **36**, 641.

Teegarden, B. J., Cline, T. L., Gehrels, N., Porreca, G., Tueller, J., Leventhal, M., Huters, A. F., MacCallum, C. J., and Stang, P. D.: 1985, *Proc. 19th Cosmic Ray Conf.*, OG 9.2–4, p. 307.

Theinhardt, J., Burk, R., Kendziorra, E., and Staubert, R.: 1984, *Nucl. Instr. Meth. Phys. Res.* **221**, 288.

Thompson, D. J.: 1986, *Nucl. Instr. Meth. Phys. Res.* **A251**, 390.

Ventura, G., Horstman, H. M., Brighenti, A., Cavani, C., Camprini, M., Cazzola, P., Giovannini, G., Labanti, C., and Poulsen, J. M.: 1984, *Nucl. Instr. Meth. Phys. Res.* **A226**, 524.

Villa, G., Bussini, A., Perotti, F., Santambrogio, R., Rampini, A., Di Cocco, G., Butler, R. C., Caroli, E., Stephen, J. B., Traci, A., Donati, A., Ubertini, P., La Padula, C., Mastropietro, M., Patriarca, R., Dean, A. J., Court, A. J., Younis, F. A., Maggioli, P., Yearworth, M., and Graham, G.: 1987, *IEEE Trans. Nucl. Sci.* **NS-34**, 26.

Willingale, R.: 1984, *Nucl. Instr. Meth. Phys. Res.* **A221**, 1.

Willingale, R., Sims, M. R., and Turner, M. J. L.: 1984, *Nucl. Instr. Meth. Phys. Res.* **A221**, 60.

Willmore, A. P., Skinner, G. K., Eyles, C. J., and Ramsey, B.: 1981, *Space Sci. Rev.* **30**, 601.

Willmore, A. P., Skinner, G. K., Eyles, C. J., and Ramsey, B.: 1984, *Nucl. Instr. Meth.* **221**, 284.

Woods, J. W., Ekstrom, M. P., Palmieri, T. M., and Twogood, R. E.: 1975, *IEEE Trans. Nucl. Sci.* **NS-22**, 379.

Yamanaka, C., Yamanaka, M., Niki, H., Yamada, A., Yamamoto, Y., and Yamanaka, T.: 1984, *IEEE Trans. Nucl. Sci.* **NS-31**, 490.